2017

Laboratory experiments of resident space object capture by a spacecraft-manipulator system

Virgili-Llop, Josep; Drew, Jerry V.; Zappulla, Richard II; Romano, Marcello

Elsevier

J. Virgili-Llop, J.V. Drew, R.Zappulla II, M. Romano, "Laboratory experiments of resident space object capture by a spacecraft-manipulator system," v.71 (2017), pp. 530-545. http://hdl.handle.net/10945/56215

Aerospace Science and Technology 71 (2017) 530–545

Contents lists available at ScienceDirect

Aerospace Science and Technology

www.elsevier.com/locate/aescte

Laboratory experiments of resident space object capture by a spacecraft–manipulator system

Josep Virgili-Llop *, Jerry V. Drew, Richard Zappulla II, Marcello Romano

Spacecraft Robotics Laboratory, Naval Postgraduate School, Monterey, CA, 93940, United States

ARTICLE INFO

Article history:
Received 6 December 2016
Received in revised form 25 May 2017
Accepted 27 September 2017
Available online 4 October 2017

Keywords:
Space robotics
Hardware-in-the-loop
Guidance and control

ABSTRACT

A set of laboratory experiments are conducted to demonstrate the autonomous capture of a simulated resident space object by a simulated spacecraft equipped with a robotic manipulator. A planar air-bearing test bed provides a quasi-weightless and drag-free dynamic environment on a plane. To control the chaser's base, floating, flying, and rotation-flying control approaches are implemented and compared. A resolved-motion-rate controller is used to control the manipulator's joints. Using these control methods a floating object at rest is successfully captured. Furthermore, the capture of a floating and rotating object is demonstrated using a flying base control approach. The originality of these experiments comes from the remarkably high dynamic coupling of the spacecraft–manipulator system used. Emphasis is given to the guidance and control problems, with the relative navigation problem being left outside the scope of this effort.

1. Introduction

Many future space missions (*e.g.*, servicing, inspection or active debris removal) may require the use of robotic manipulators to capture cooperative or non-cooperative Resident Space Objects (RSO). The dynamics of space-based manipulators substantially differ from their terrestrial counterparts, as the base-spacecraft, not being anchored to the ground, is free to react to the manipulator's motion. The effects of this dynamic coupling intensify as the base-spacecraft to manipulator mass and inertia ratios decrease. Adding onto the inherently nonlinear manipulator dynamics, systems that exhibit a large dynamic coupling present a particularly challenging modeling and control problem. Other hardware related non-linearities (*e.g.*, contact dynamics, friction, structural flexibility, joint backlash or signal time delays) further magnify the challenge.

Extensive analytic work and numerical simulations have been devoted to the modeling and control of spacecraft–manipulator systems, chiefly focusing on RSO capture [1–3]. The scarcity of suitable test facilities to recreate the complex dynamic phenomena [4,5] has made the equivalent experimental-based work exceedingly rare [6–15].

The growing interest and adoption of small spacecraft has stimulated multiple mission designs that feature robotic manipulators mounted on small spacecraft, which result in highly coupled systems [16–19]. The dynamic complexity of these space-robotic systems, difficult to recreate in a numerical simulation environment, justifies the use of high fidelity experimental facilities to validate, verify and demonstrate the feasibility of robotic spacecraft maneuvering for this class of highly coupled systems [20].

In this paper, the autonomous capture of an RSO by a spacecraft–manipulator system with a large dynamic coupling is demonstrated in a laboratory environment. Floating, flying, and rotation-flying base-spacecraft control approaches have been experimentally demonstrated and compared. This demonstration exclusively focuses on the guidance and control problems and has been carried out in a test facility that replicates the drag-free and weightless conditions of spaceflight. The dynamic fidelity of the test bed, combined with the hardware related effects of the test vehicles, provide a level of realism remarkably difficult to recreate in a numerical simulation setup.

The POSEIDYN[1] air-bearing test bed [21] is used here to provide a quasi-frictionless and weightless dynamic environment on a plane. To achieve these dynamic properties, the test vehicles float, via planar air bearings, over a horizontally leveled 4-by-4 meter granite table. The chaser's spacecraft–manipulator system is composed of a Floating Spacecraft Simulator (FSS), acting as the base-spacecraft, and a four-link kinematically redundant robotic manipulator. To generate the requested forces and torques the chaser base-spacecraft is equipped with eight cold-gas thrusters and a reaction wheel. A second FSS is used to simulate the RSO to be

* Corresponding author.
E-mail address: jvirgili@nps.edu (J. Virgili-Llop).

[1] POSEIDYN is a backronym standing for Proximity Operation of Spacecraft: Experimental hardware-In-the-loop DYNamic simulator.

https://doi.org/10.1016/j.ast.2017.09.043
1270-9638/

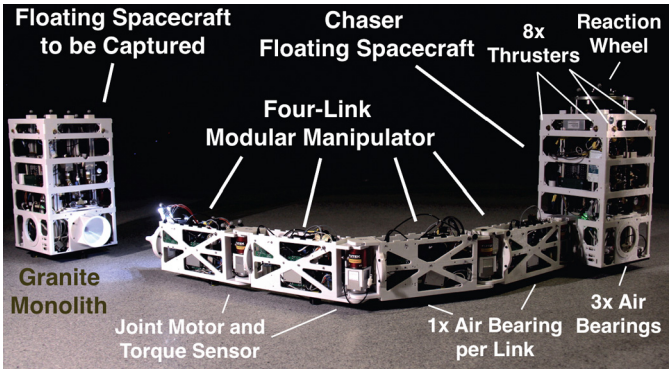

Fig. 1. Target and chaser FSS with robotic manipulator in the POSEIDYN test bed at the Spacecraft Robotics Laboratory.

captured and an overhead motion capture system is used to determine the position and orientation of the test vehicles. See Fig. 1 for an overview of the experimental setup. The experiments presented here are a continuation of an earlier set of experiments conducted by the authors in the POSEIDYN test bed [22].

Previously flown and experimentally tested spacecraft–manipulator systems have exhibited substantially more benign mass and inertia ratios than the ones found in the spacecraft–manipulator system used for this set of experiments. The Space Shuttle orbiters with their Shuttle Remote Manipulator System [23], the International Space Station (ISS) with its Space Station Remote Manipulator System [24], the ETS-VII [25], and the Orbital Express [26,27] exhibited mass ratios ranging from $\sim$222 for the ISS down to $\sim$15 for the Orbital Express mission.

Laboratory-based hardware-in-the-loop systems have gone down to mass ratios of 2.2. Of particular importance are the experiments of Umetani and Yoshida, who demonstrated the capture of static and moving objects using a spacecraft–manipulator system with a single two-link manipulator with a mass ratio of 4.5 [7,11]. More recently, the Space Research Centre of the Polish Academy of Sciences experimentally demonstrated the controllability of a two-link system with a mass ratio of 2.15 [20].

The distinctive aspect of these experiments presented here is the relatively small base-spacecraft used (in terms of mass and inertia). With a base-spacecraft to manipulator mass ratio of $\approx$1 and an inertia ratio of $\approx$1/50 (with a fully extended manipulator), the dynamic coupling of the system is remarkably prominent. Furthermore, the four-link kinematically redundant manipulator also represents an increase on the dynamic complexity with respect to past laboratory-based experiments. In summary, the experiments presented here advance the experimentally demonstrated state-of-the-art of robotic spacecraft maneuvering.

The rest of this paper is organized as follows. The considered capture scenarios are presented in Section 2. Then, the proposed guidance and control laws are presented and discussed in Section 3. A detailed overview of the experimental setup is provided in Section 4. Finally, in Section 5 the experimental and numerical simulation results are presented, and in Section 6, these are analyzed and discussed.

2. Test scenario

For the experimental demonstration two distinct scenarios have been considered. The first involves a floating RSO at rest, while the second considers a floating and rotating RSO.

The RSO at rest case represents a scenario where the target RSO maintains a constant and fixed attitude and position. This is experimentally achieved by having the target FSS floating over the granite monolith while using its onboard thrusters to keep its position and orientation. In the rotating RSO scenario, the target RSO orientation changes at a constant rate. In this instance, the target FSS also controls its position, orientation, and angular rate using its onboard thrusters. As both the chaser and target FSS are floating on the granite table, the contact dynamics experienced during the capture maneuver will have a disturbing effect on their positions and orientations.

The final close-in approach to the RSO and its subsequent capture are the only maneuver phases considered and experimentally evaluated in this study (*i.e.*, far range rendezvous is ignored). During these final phases, the double integrator dynamics provided by the POSEIDYN test bed are an acceptable approximation to the real relative dynamics between two orbiting vehicles. In fact, when the chaser and the target RSO remain in close proximity and the maneuver duration is small when compared to the orbital period, the effects of the relative orbital dynamics can be treated as negligible perturbations.

3. Design and analysis of the guidance and control laws

To achieve the capture of the target FSS, a four-phased maneuver is adopted. Fig. 2 notionally shows these phases.

Ph.1 *Initial approach phase* (fly to initial hold position). The chaser closes in on the target FSS, adopting a hold position in its proximity. During this initial maneuver the manipulator is in a folded configuration, minimizing the vehicle's overall inertia and enhancing its maneuverability.

Ph.2 *Manipulator unfolding phase*. The chaser's manipulator is unfolded, adopting its pre-capture configuration. During the unfolding maneuver, the base-spacecraft is not controlled, leaving the base-spacecraft to freely react to the manipulator's motion and saving control effort. This base reaction is precomputed and accounted for when selecting the initial hold position (at the end of *Ph*.1). The goal is to have the chaser directly facing the target after the unfold maneuver is completed.

Ph.3 *Final approach phase* (fly to pre-capture hold position). The chaser moves to the pre-capture hold position, refining its alignment and bringing the target FSS within a predetermined capture range.

Ph.4 *Capture phase*. The chaser captures the target FSS by extending its robotic manipulator and using the base-spacecraft actuators. Ideally, the pre-capture hold position at the end of *Ph*.3, allows the manipulator's to capture the target FSS by moving its end-effector in a straight line.

Note that in Fig. 2, as well as in subsequent figures, the black cross indicates the location of the chaser's Center-of-Mass (CoM) and the dashed line indicates its trajectory.

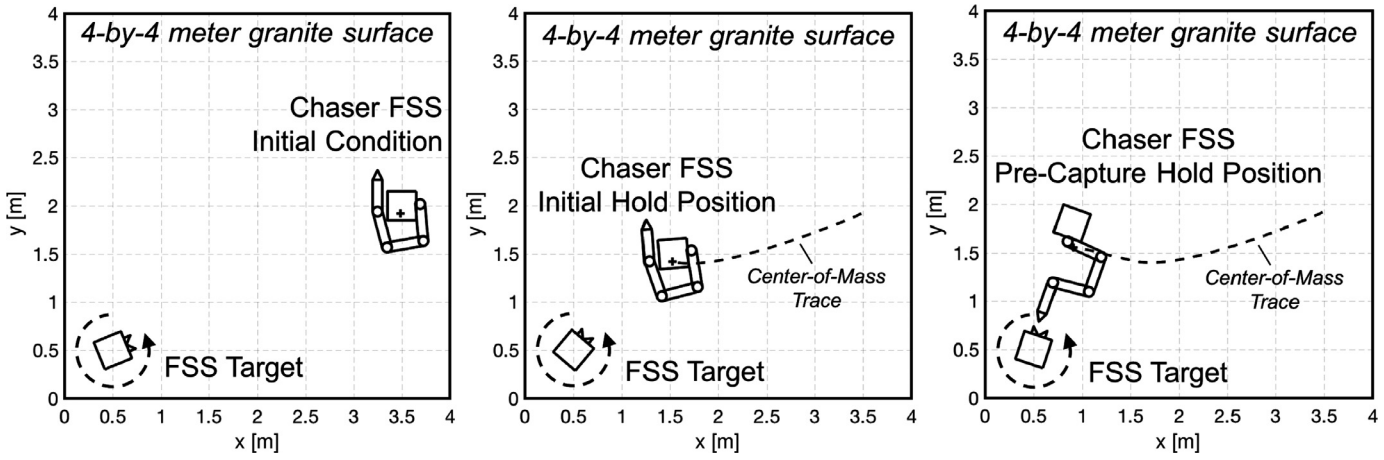

(a) Initial condition (b) Initial hold (end of *Ph*.1) (c) Pre-capture hold (end of *Ph*.3)

Fig. 2. Notional sequence used in the capture of the target FSS on the POSEIDYN test bed.

In the rotating target case, the pre-capture hold position to be adopted at the end of *Ph*.3 is not fixed, but rather tracks the rotating target, with the chaser FSS describing a circular trajectory around it (see Fig. 2). This strategy allows to capture the target by moving the end-effector in a straight line, retaining the commonality between the rotating target and target at rest scenarios.

The four phased approach proposed here is certainly not the only one possible. More complex and propellant-optimal strategies, using optimization-based guidance, have been proposed [28–33], although not experimentally demonstrated yet.

3.1. Equations of motion

Before describing the different guidance and control strategies used during the four different phases, let's briefly introduce the equations of motion of a spacecraft–manipulator system and present the nomenclature that will be used in following sections.

The equations of motion of a robotic multibody system with a moving base can be written as in Eq. (1), with $\boldsymbol{H}$ denoting the generalized inertia matrix, $\boldsymbol{C}$ the generalized convective inertia matrix (Coriolis and centrifugal forces), and $\boldsymbol{\tau}$ the generalized forces acting on the system. The vector $\boldsymbol{q}$ denotes the generalized variables of the system, representing a convenient set of variables that fully describe the state of the multibody system. The generalized forces $\boldsymbol{\tau}$ are the forces that act upon these generalized variables $\boldsymbol{q}$.

$$\boldsymbol{H}(\boldsymbol{q})\ddot{\boldsymbol{q}} + \boldsymbol{C}(\boldsymbol{q},\dot{\boldsymbol{q}})\dot{\boldsymbol{q}} = \boldsymbol{\tau} \tag{1}$$

The generalized variables $\boldsymbol{q}$ can be decomposed $\boldsymbol{q} = [\boldsymbol{q}_0\, \boldsymbol{q}_m]^T$ into base-spacecraft variables $\boldsymbol{q}_0$, containing the position and orientation of the base, and manipulator related variables $\boldsymbol{q}_m$, containing the manipulator's joint angular displacements. Using this decomposition, the equations of motion can be expanded as shown in Eq. (2). The generalized forces can also be decomposed $\boldsymbol{\tau} = [\boldsymbol{\tau}_0\, \boldsymbol{\tau}_m]^T$ into base-spacecraft forces and torques $\boldsymbol{\tau}_0$ and torques acting on the manipulator joints $\boldsymbol{\tau}_m$.

$$\begin{bmatrix} \boldsymbol{H}_0 & \boldsymbol{H}_{0m} \\ \boldsymbol{H}_{0m}^T & \boldsymbol{H}_m \end{bmatrix} \begin{bmatrix} \ddot{\boldsymbol{q}}_0 \\ \ddot{\boldsymbol{q}}_m \end{bmatrix} + \begin{bmatrix} \boldsymbol{C}_0 & \boldsymbol{C}_{0m} \\ \boldsymbol{C}_{m0} & \boldsymbol{C}_m \end{bmatrix} \begin{bmatrix} \dot{\boldsymbol{q}}_0 \\ \dot{\boldsymbol{q}}_m \end{bmatrix} = \begin{bmatrix} \boldsymbol{\tau}_0 \\ \boldsymbol{\tau}_m \end{bmatrix} \tag{2}$$

The $\boldsymbol{H}_{0m}$ term conveys the dynamic coupling of the system. Numerically large values in the elements of $\boldsymbol{H}_{0m}$ reveal a strong dynamic coupling between the base and the manipulator.

In the planar, two translation and one rotation degree-of-freedom environment of the POSEIDYN test bed, the base-spacecraft's variables $\boldsymbol{q}_0$ and forces $\boldsymbol{\tau}_0$, are defined as follows:

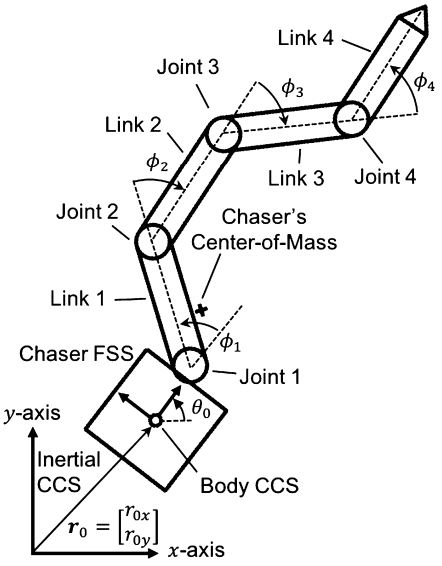

Fig. 3. Illustration of the chaser FSS and its robotic manipulator.

$$\boldsymbol{q}_0 = \begin{bmatrix} r_{0x} \\ r_{0y} \\ \theta_0 \end{bmatrix} \quad \dot{\boldsymbol{q}}_0 = \begin{bmatrix} \dot{r}_{0x} \\ \dot{r}_{0y} \\ \dot{\theta}_0 \end{bmatrix} \quad \ddot{\boldsymbol{q}}_0 = \begin{bmatrix} \ddot{r}_{0x} \\ \ddot{r}_{0y} \\ \ddot{\theta}_0 \end{bmatrix} \quad \boldsymbol{\tau}_0 = \begin{bmatrix} F_{0x} \\ F_{0y} \\ n_0 \end{bmatrix} \tag{3}$$

With r_{0x}, r_{0y}, θ_0 denoting, as shown in Fig. 3, the base-spacecraft position and orientation with respect to an inertial Cartesian Coordinate System (CCS), respectively. The external forces acting on the base-spacecraft are denoted by F_{0x} and F_{0y}, and the torque by n_0.

As the manipulator mounted on the FSS has four links connected by four joints, the manipulator's variables $\boldsymbol{q}_m$ and associated forces $\boldsymbol{\tau}_m$ can be simply written as in Eq. (4), with ϕ_i and n_i respectively denoting the angular displacement of and torque acting on the ith joint.

$$\boldsymbol{q}_m = \begin{bmatrix} \phi_1 \\ \phi_2 \\ \phi_3 \\ \phi_4 \end{bmatrix} \quad \boldsymbol{\tau}_m = \begin{bmatrix} n_1 \\ n_2 \\ n_3 \\ n_4 \end{bmatrix} \tag{4}$$

The location of the system's center-of-mass $\boldsymbol{r}_{\text{CoM}}$ is computed as:

$$\boldsymbol{r}_{\text{CoM}} = \frac{\sum_{i=0}^{i=4} \boldsymbol{r}_i m_i}{\sum_{i=0}^{i=4} m_i} = \begin{bmatrix} r_{x,\text{CoM}} \\ r_{y,\text{CoM}} \end{bmatrix} \tag{5}$$

with m_i and $\boldsymbol{r}_i = f(\boldsymbol{q})$ denoting the mass and the center-of-mass position of each of the bodies, respectively.

To derive the kinematic and dynamic magnitudes of the spacecraft–manipulator system the open source SPacecraft Robotics Toolkit (SPART) is used [34,35]. This toolkit generates the kinematic and dynamic models that are executed in real-time on the spacecraft–manipulator system onboard computer. During the experiments, these models are re-computed at a frequency of 50 Hz.

The spacecraft–manipulator kinematic and dynamic primitives (*i.e.*, geometry, mass and inertia of the different bodies) were previously determined by direct measurement or via a dynamic and kinematic calibration [36]. The kinematic calibration allows the system to determine the end-effector's position and orientation, from the joint displacement $\boldsymbol{q}_m$ and base-spacecraft state $\boldsymbol{q}_0$, with a 1σ uncertainty of 1.8 mm in position and 0.36° in orientation.

With the dynamics of the system covered, the multiple guidance and control laws used for the different phases of the capture maneuver can be presented.

3.2. Ph.1 and Ph.3 translation and rotation controller

During the first and third phases, the chaser spacecraft–manipulator system flies to a hold position, conducting a system-wide translation and rotation with a constant manipulator configuration ($\dot{\boldsymbol{q}}_m = \ddot{\boldsymbol{q}}_m = 0$).

To control these maneuvers, a Linear-Quadratic Regulator (LQR) is used. LQR controllers have been proposed for spacecraft proximity maneuvering and successfully demonstrated in the POSEIDYN test bed [37] and during on-orbit demonstrations [38].

The LQR controller determines the forces and torques to be imparted on the base-spacecraft $\boldsymbol{\tau}_0$. The manipulator joints are commanded to hold their state ($\dot{\boldsymbol{q}}_m = \ddot{\boldsymbol{q}}_m = 0$). To formulate the LQR, a state-space representation of the system's dynamics is required.

$$\dot{\boldsymbol{x}} = \boldsymbol{A}\boldsymbol{x} + \boldsymbol{B}\boldsymbol{u} \tag{6a}$$

$$\boldsymbol{x} = \begin{bmatrix} \boldsymbol{q}_0 \\ \dot{\boldsymbol{q}}_0 \end{bmatrix} \tag{6b}$$

$$\boldsymbol{u} = \boldsymbol{\tau}_0 \tag{6c}$$

The state matrix $\boldsymbol{A}$ and input matrix $\boldsymbol{B}$ defined, using Eq. (2), as follows:

$$\boldsymbol{A} = \begin{bmatrix} \boldsymbol{0}_{3\times3} & \boldsymbol{I}_{3\times3} \\ \boldsymbol{0}_{3\times3} & -\boldsymbol{H}_0^{-1}\boldsymbol{C}_0 \end{bmatrix} \tag{7a}$$

$$\boldsymbol{B} = \begin{bmatrix} \boldsymbol{0}_{3\times3} \\ \boldsymbol{H}_0^{-1} \end{bmatrix} \tag{7b}$$

where $\boldsymbol{I}_{3\times3}$ and $\boldsymbol{0}_{3\times3}$ denote a 3×3 identity and zero matrix, respectively.

During these maneuvers, the manipulator configuration remains constant, making the inertia matrix $\boldsymbol{H}_0$ a constant. In contrast, the convective inertia matrix is a function of the base-spacecraft angular velocity $\boldsymbol{C}_0 = f(\dot{\boldsymbol{q}}_0)$ and is not constant. As defined, the system is in effect nonlinear. A State-Dependent Riccati Equation (SDRE) technique could be used to design a nonlinear regulator [39].

To obtain an Linear Time-Invariant (LTI) system, and simplify the design of the LQR controller, the $\boldsymbol{H}_0^{-1}\boldsymbol{C}_0$ term is neglected, resulting in the following simplified state matrix:

$$\boldsymbol{A} \approx \begin{bmatrix} \boldsymbol{0}_{3\times3} & \boldsymbol{I}_{3\times3} \\ \boldsymbol{0}_{3\times3} & \boldsymbol{0}_{3\times3} \end{bmatrix} \tag{8}$$

This simplification is justified because the terminal conditions of *Ph.*1 and *Ph.*3 are hold positions with zero velocities (or small velocities in the rotating target case).

$$\dot{\boldsymbol{q}} \approx \boldsymbol{0} \Longrightarrow \boldsymbol{C}_{0m} \approx \boldsymbol{0} \tag{9}$$

Table 1
Numerical values for the Linear-Quadratic Regulator state $\boldsymbol{Q}$ and control $\boldsymbol{R}$ weight matrices.

Matrix	Values
*Ph.*1 $\boldsymbol{Q}$	$\mathrm{diag}\left[1/0.04^2, 1/0.04^2, 1/0.0175^2, 1/0.001^2, 1/0.001^2, 1/0.0349^2\right]$
*Ph.*1 $\boldsymbol{R}$	$1000 \cdot \mathrm{diag}\left[1/0.30^2, 1/0.30^2, 1/0.12^2\right]$
*Ph.*3 $\boldsymbol{Q}$	$\mathrm{diag}\left[1/0.01^2, 1/0.01^2, 1/0.0175^2, 1/0.001^2, 1/0.001^2, 1/0.0087^2\right]$
*Ph.*3 $\boldsymbol{R}$	$800 \cdot \mathrm{diag}\left[1/0.30^2, 1/0.30^2, 1/0.12^2\right]$
*Ph.*4 $\boldsymbol{Q}$	$\mathrm{diag}\left[1/0.01^2, 1/0.01^2, 1/0.0175^2, 1/0.005^2, 1/0.005^2, 1/0.0175^2\right]$
*Ph.*4 $\boldsymbol{R}$	$1000 \cdot \mathrm{diag}\left[1/0.30^2, 1/0.30^2, 1/0.12^2\right]$

Table 2
State error tolerance to transition between maneuver phases.

Hold	State tolerance $\boldsymbol{x}_{\mathrm{tol}}$
Hold at end *Ph.*1	$\boldsymbol{x}_{\mathrm{tol}} = [10\ \mathrm{cm}, 10\ \mathrm{cm}, 5°, 1\ \mathrm{cm/s}, 1\ \mathrm{cm/s}, 1°/\mathrm{s}]$
Hold at end *Ph.*3	$\boldsymbol{x}_{\mathrm{tol}} = [5\ \mathrm{cm}, 5\ \mathrm{cm}, 1°, 0.5\ \mathrm{cm/s}, 0.5\ \mathrm{cm/s}, 0.5°/\mathrm{s}]$

Another option to simplify the system is to formulate the equations of motion from the system's center-of-mass [22], directly obtaining a linear system.

The performance measure of an infinite-horizon LQR can be written as in Eq. (10), with $\boldsymbol{Q}$ and $\boldsymbol{R}$ denoting the state weighting matrix and the control weighting matrix, respectively.

$$J_{\mathrm{cost}} = \int_0^\infty \left(\boldsymbol{x}^T\boldsymbol{Q}\,\boldsymbol{x} + \boldsymbol{u}^T\boldsymbol{R}\boldsymbol{u}\right) dt \tag{10}$$

The manipulator's configuration during *Ph.*1 (folded) is different than the one during *Ph.*3 (unfolded), resulting in different inertia matrices $\boldsymbol{H}_0$ and different LTI systems. The different requirements for *Ph.*1 and *Ph.*3 may also lead to different $\boldsymbol{Q}$ and $\boldsymbol{R}$ weight matrices. These differences between the two different approach phases result in different, yet constant, LQR gains $\boldsymbol{K}$.

The numerical values of the state weighting matrix $\boldsymbol{Q}$ and the control weighting matrix $\boldsymbol{R}$ used during the experimental campaign are provided in Table 1 (these values assume SI units in the state $\boldsymbol{x}$ and control $\boldsymbol{u}$ vectors). The heuristic approach of setting the $\boldsymbol{Q}$ weights proportional to $1/x_\epsilon^2$ (with x_ϵ being a level of accepted error in that state) and the $\boldsymbol{R}$ weights proportional to $1/u_\epsilon^2$ (with u_ϵ being the maximum available control) are used, with these weights ultimately adjusted by trial and error during preliminary numerical simulation efforts.

Phases one, *Ph.*1, and three, *Ph.*3, end with the chaser FSS in a hold position. This hold positions are assumed to be reached when the FSS state error is below a certain tolerance $\boldsymbol{x}_e \leq \boldsymbol{x}_{\mathrm{tol}}$, where $\leq$ denotes an element-wise relational operator that is true when all the elements meet their respective inequality condition.

$$\boldsymbol{x}_e = \boldsymbol{x}_{\mathrm{hold}} - \boldsymbol{x} \tag{11a}$$

$$\boldsymbol{x}_{\mathrm{hold}} = \begin{bmatrix} \boldsymbol{q}_{0,\mathrm{hold}} \\ \boldsymbol{0}_{3\times1} \end{bmatrix} \tag{11b}$$

When this tolerance is met, the chaser transitions to the next maneuver phase. The tolerances used in the experimental campaign $\boldsymbol{x}_{\mathrm{tol}}$ are presented in Table 2. A tighter tolerance is justified on the pre-capture hold position (end of *Ph.*3) as the final capture maneuver, requiring a good alignment and positioning, follows. How the hold positions $\boldsymbol{q}_{0,\mathrm{hold}}$ are obtained is discussed in Section 3.5.

3.3. Ph.2 manipulator unfold controller

During the manipulator unfolding phase *Ph.*2, the manipulator is, from its stowed configuration, unfolded into its pre-capture configuration (see Fig. 2). To avoid using additional propellant, the base-spacecraft is left uncontrolled (floating) while the manipulator is unfolded. The base-spacecraft's reaction during the unfold

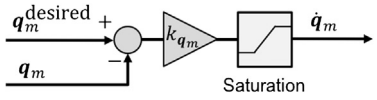

Fig. 4. Controller used for the manipulator unfolding maneuver.

Table 3
Manipulator Unfold and Resolved-Motion-Rate controller parameters.

Parameter	Value
Manipulator Unfold Controller	
Proportional gain k_{q_m}	0.5
Manipulator saturation velocity	20°/s
$\lvert q_m^{\text{desired}} - q_m \rvert$ to complete maneuver	≤1°
Resolved-Motion-Rate Controller	
Proportional gain k_{rmr}	0.5
Traverse velocity of q_{EE}^{desired}	1 cm/s
End-effector error to finish maneuver	≤1 mm

maneuver is taken into account when determining the *Ph*.1 hold position, so after the unfold maneuver is completed, the chaser is correctly aligned and positioned.

To estimate this base reaction, the system's momenta is analyzed. If the top half of the left-hand side of the equation of motion Eq. (2) is integrated, the momentum equation, shown in Eq. (12) is obtained. In this equation, $\mathcal{M}$ denotes the system momenta (both linear and angular).

$$\boldsymbol{H}_0\dot{\boldsymbol{q}}_0 + \boldsymbol{H}_{0m}\dot{\boldsymbol{q}}_m = \mathcal{M} \tag{12}$$

The base-reaction can be estimated using the expression on Eq. (12), if the evolution of the momenta is known.

$$\dot{\boldsymbol{q}}_0 = -\boldsymbol{H}_0^{-1}\left(\boldsymbol{H}_{0m}\dot{\boldsymbol{q}}_m - \mathcal{M}\right) \tag{13}$$

If the unfold maneuver is initiated with the spacecraft–manipulator system at rest and leaving the base-uncontrolled—no momentum exchange—the momenta is kept constant at $\mathcal{M} = 0$. These assumptions allow to compute the base-spacecraft reaction as follows:

$$\dot{\boldsymbol{q}}_0 = -\boldsymbol{H}_0^{-1}\left(\boldsymbol{H}_{0m}\dot{\boldsymbol{q}}_m\right) \tag{14}$$

This last expression is used to estimate, *a priori*, the base-spacecraft reaction during the unfold maneuver. This reaction is accounted for when determining the *Ph*.1 hold position and orientation.

For the unfold maneuver, the proportional controller shown in Fig. 4 is used. In this controller, $\boldsymbol{q}_m^{\text{desired}}$ denotes the desired manipulator configuration and $k_{\boldsymbol{q}_m}$ denotes the controller's proportional gain. The output of the controller is a commanded joint velocity $\dot{\boldsymbol{q}}_m$, which is limited to ±20°/s. The unfolding maneuver is considered complete when $\lvert \boldsymbol{q}_m^{\text{desired}} - \boldsymbol{q}_m \rvert \leq 1°$. The manipulator unfold controller parameters are provided in Table 3.

3.4. Ph.4 final capture phase controller

The following control strategies have been explored for the final capture phase *Ph*.4:

- *Ctr*.1 Floating base (base-spacecraft freely reacting) with a manipulator resolved-motion-rate control.
- *Ctr*.2 Flying base (base-spacecraft position and attitude controlled) with a manipulator resolved-motion-rate control.
- *Ctr*.3 Rotation-flying base (base-spacecraft attitude controlled) with a manipulator resolved-motion-rate control.

3.4.1. Resolved-motion-rate control

For all the different base-control strategies during *Ph*.4, the manipulator is controlled using a resolved-motion-rate controller [40,41]. In this controller, the differential kinematic relationship between the spacecraft–manipulator system and the manipulator's end-effector is exploited to determine the required joint motion that produces a desired end-effector motion.

The differential kinematic relationship can be expressed through the base and manipulator Jacobians, which map the joint space velocities of the manipulator $\dot{\boldsymbol{q}}_m$ and the base $\dot{\boldsymbol{q}}_0$, to the operational space velocities (linear and angular) of the end-effector $\boldsymbol{t}_{EE}$.

$$\boldsymbol{t}_{EE} = \begin{bmatrix} \dot{r}_{EEx} \\ \dot{r}_{EEy} \\ \dot{\theta}_{EE} \end{bmatrix} \tag{15a}$$

$$\boldsymbol{t}_{EE} = \boldsymbol{J}_0(\boldsymbol{q})\,\dot{\boldsymbol{q}}_0 + \boldsymbol{J}_m(\boldsymbol{q})\,\dot{\boldsymbol{q}}_m \tag{15b}$$

This relationship is exploited to obtain the required manipulator joint velocities $\dot{\boldsymbol{q}}_m$ that provide the desired end-effector motion $\boldsymbol{t}_{EE}^{\text{desired}}$ for a given base-spacecraft motion $\dot{\boldsymbol{q}}_0$.

As the vehicle operates in a planar three degrees-of-freedom environment, the manipulator's four degrees-of-freedom provide kinematic redundancy. As a result, the manipulator Jacobian $\boldsymbol{J}_m$ is not square and cannot be directly inverted. The Moore-Penrose pseudoinverse $\boldsymbol{J}_m^+$ is used to obtain the solution minimizing the norm of the joint angular velocities $\dot{\boldsymbol{q}}_m$. This minimum-rate resolved-motion-rate controller is the one that has been implemented and takes the following form:

$$\dot{\boldsymbol{q}}_m = \boldsymbol{J}_m^+\left(\boldsymbol{t}_{EE}^{\text{desired}} - \boldsymbol{J}_0\dot{\boldsymbol{q}}_0\right) \tag{16a}$$

$$\boldsymbol{J}_m^+ = \boldsymbol{J}_m^T\left(\boldsymbol{J}_m\boldsymbol{J}_m^T\right)^{-1} \tag{16b}$$

The motion of the base $\dot{\boldsymbol{q}}_0$, required in Eq. (16) to obtain the required manipulator motion, can either be measured or predicted (*e.g.*, using the expression in Eq. (13)). During the experimental campaign the base motion $\dot{\boldsymbol{q}}_0$ is determined by the onboard navigation filter.

Although the manipulator's kinematic redundancy is used to obtain minimum joint rates, it could also be exploited to accomplish a different objective. For example, the manipulator's kinematic redundancy creates a null-space that can be exploited to re-configure the manipulator without affecting the end-effector position with respect to the base. This can be used to eliminate the base reaction, as used in the Zero-Reaction-Maneuver approach [42], or, in general, to minimize any other cost function [43].

For the experimental implementation of the resolved-motion-rate control, a proportional controller with a k_{rmr} gain and driven by the difference between the current end-effector state $\boldsymbol{q}_{EE}^{\text{current}}$ with respect to the desired one $\boldsymbol{q}_{EE}^{\text{desired}}$, is used to determine the desired end-effector velocity $\boldsymbol{t}_{EE}^{\text{desired}}$ later used in Eq. (16).

$$\boldsymbol{t}_{EE}^{\text{desired}} = k_{\text{rmr}}\left(\boldsymbol{q}_{EE}^{\text{desired}} - \boldsymbol{q}_{EE}^{\text{current}}\right) \tag{17a}$$

$$\boldsymbol{q}_{EE} = \begin{bmatrix} r_{EEx} \\ r_{EEy} \\ \theta_{EE} \end{bmatrix} \tag{17b}$$

For the experimental campaign a $k_{\text{rmr}} = 0.5$ is used. This k_{rmr} value offered a good tracking accuracy while not overreacting to the noise present on $\boldsymbol{q}_{EE}^{\text{current}}$. The noise in $\boldsymbol{q}_{EE}^{\text{current}}$ originates in the raw joint angular displacement $\boldsymbol{q}_m$ measurements and the navigation filter estimates of the base-spacecraft position $\boldsymbol{q}_0$.

Nominally, when the final capture phase starts, the end-effector is aligned with the target and thus the end-effector only needs to move in a straight line to capture it. To compensate for errors, the end-effector chases a desired end-effector state $\boldsymbol{q}_{EE}^{\text{desired}}$, gradually moving from its initial (nominal) position to its final capture position. The errors are then compensated by the proportional controller in Eq. (17). This concept is notionally shown in Fig. 5.

The desired end-effector state $\boldsymbol{q}_{EE}^{\text{desired}}$ that the end-effector chases moves at a constant 1 cm/s. This velocity ensures that the

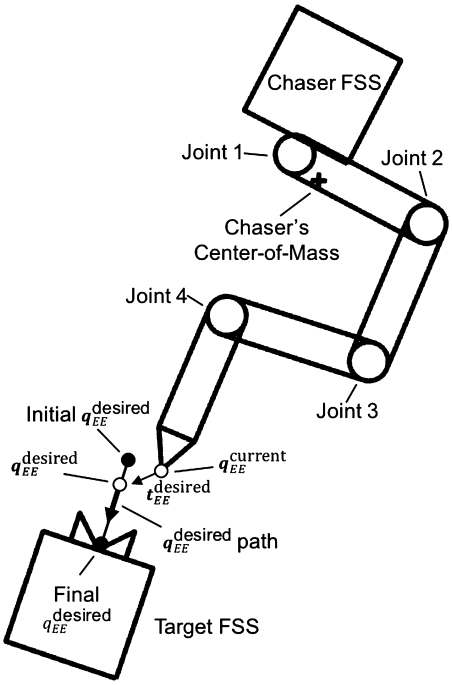

Fig. 5. During the capture maneuver (*Ph.*4), the manipulator's end-effector $\boldsymbol{q}_{EE}^{\text{current}}$ chases a moving desired end-effector state $\boldsymbol{q}_{EE}^{\text{desired}}$.

target will be captured in a timely manner, while limiting the instantaneous base reaction to the manipulator's motion. The capture maneuver is considered complete when the end-effector is within 1 mm of its target.

A summary of the parameters used for the resolved-motion-rate controller can be found in Table 3. The different base-spacecraft control modes are now presented.

3.4.2. Ctr.1—floating base

In this mode, the base-spacecraft is left uncontrolled, freely reacting to the manipulator's motion. In a floating "control" mode, the uncontrolled base reaction limits the end-effector range. Fig. 6(a) shows the initial configuration that offers the "largest" straight-line end-effector range with a minimum-rate resolved-motion-rate controller. The maneuver range and the base reaction, in terms of position $\|\Delta \boldsymbol{r}_0\|$ and orientation $\Delta\theta_0$ displacement, as well as the final extended configuration (dashed spacecraft–manipulator) are also shown in Fig. 6(a). The center-of-mass of the system in its initial configuration is marked with a cross, while the center-of-mass of the final extended configuration is marked with a circle. As expected, in the floating case, the initial and final center-of-mass are coincident (as no linear momentum is imparted to the system). In Fig. 6, a symmetric configuration with respect to the first joint also offers the same straight-line end-effector range.

The configurations shown in Fig. 6 have been obtained via an exhaustive search of the straight-line range offered by a finite set of initial manipulator configurations. The searched set is constructed as a grid of equally spaced manipulator configurations (in terms of joint displacements). Seven different displacements per joint have been considered, resulting in a total of $6^4 = 1296$ different configurations. In order to avoid redundant results, only positive angular displacements were considered for the first joint. To refine the results, a gradient-based optimization algorithm [44] was attempted but abandoned. This particular optimization method delivered, during preliminary tests, marginal gains, in terms of extra range, and proved to be too computationally intensive for practical use. The exhaustive search on a finite grid provides acceptable results at much lower computational cost, allowing to quickly recompute the initial configurations as the parameters change or as the control laws are designed and refined.

3.4.3. Ctr.2—flying base

In this case, the base-spacecraft is controlled to maintain a fixed orientation and position, counteracting any manipulator-induced reaction. The equation of motion in Eq. (2) is used to determine the base-spacecraft forces and torque $\boldsymbol{\tau}_0$ required to keep the base stable $\ddot{\boldsymbol{q}}_0 = \dot{\boldsymbol{q}}_0 = 0$.

$$\boldsymbol{H}_{0m}\ddot{\boldsymbol{q}}_m + \boldsymbol{C}_{0m}\dot{\boldsymbol{q}}_m = \boldsymbol{\tau}_0 \tag{18}$$

Under ideal conditions, applying the $\boldsymbol{\tau}_0$ resulting from Eq. (18) is enough to keep the base-spacecraft stable. Model inaccuracies, actuator uncertainties, and measurement noise eventually cause the base-spacecraft to drift. To compensate this drift an LQR controller is used. The resultant controller is notionally shown in Fig. 7 and can be seen as an LQR with the results of Eq. (18) used in a feed-forward arrangement. To simplify the design of LQR controller, a fixed manipulator configuration, corresponding to the pre-capture configuration, is considered (making $\boldsymbol{H}_0$ constant). The LQR gains are the same as the ones used during *Ph.*3, with $\boldsymbol{x}_{\text{desired}}$ being the hold position at the end of *Ph.*3.

The initial configuration that maximizes the end-effector's range when using a flying base is shown in Fig. 6(b). Note that, as a linear momentum is imparted to the system, the system's center-of-mass is displaced during the execution of the capture maneuver.

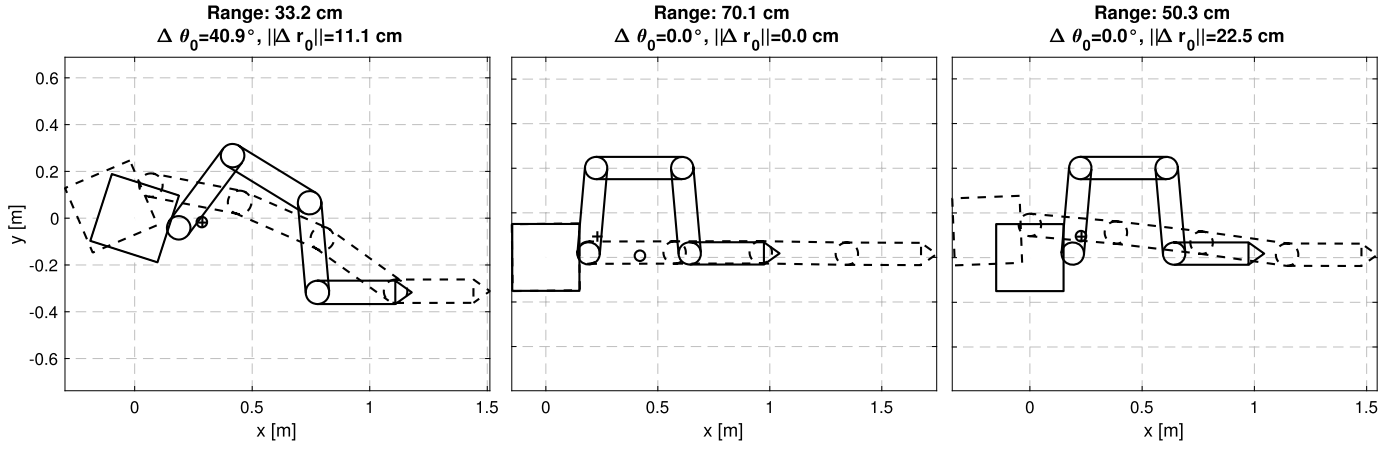

(a) Floating (b) Flying (c) Rotation-Flying

Fig. 6. Manipulator configurations with "maximum" end-effector straight-line range.

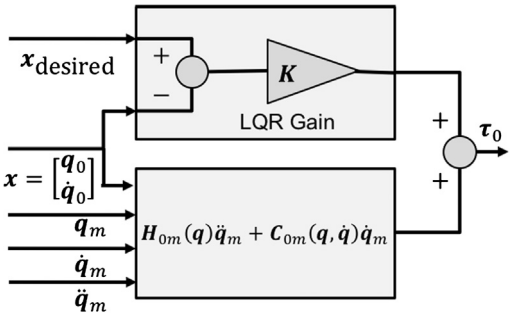

Fig. 7. LQR controller with the feed-forward used to keep the base-spacecraft stable when using a flying or rotation-flying base.

Table 4
Manipulator unfolded configurations.

Parameter	Value
Floating	$\boldsymbol{q}_m = [71.2°, 85°, -53.4°, 85°]$
Flying	$\boldsymbol{q}_m = [85°, -85°, -85°, 85°]$
Rotation-flying	$\boldsymbol{q}_m = [85°, -85°, -85°, 85°]$

Unlike the floating case, propellant is required to maintain the base-spacecraft position. This makes the flying-base control more expensive. This drawback is compensated by the significantly greater manipulator range, which allows the FSS to start the capture maneuver at a larger distance. In an actual on-orbit demonstration, special precaution needs to be exercised when using the thrusters in close proximity of the target, as the thruster plumes could potentially damage the target, contaminate its surfaces, or disturb its state through plume impingement [45].

3.4.4. Ctr.3—rotation-flying base

In this mode, the base-spacecraft is controlled to maintain its orientation, while its position is left to freely react to the manipulator's motion. This can be accomplish by the same controller used for the flying-base control mode *Ctr*.3 but only actuating the torque n_0.

The initial configuration that maximizes the end-effector's range for this control mode is shown in Fig. 6(c). In this case, no linear momentum is imparted and, as in the floating-base case, the center-of-mass remains fixed during the maneuver.

A rotation-flying control mode is in between the floating and flying control modes in terms of performance (range) and control effort. When compared to the floating-base performance, maintaining the base-spacecraft orientation significantly increases the maneuver range (although not reaching the range achieved with a flying base). As the orientation is the only controlled state, the required control effort is reduced when compared to a flying-base control. Additionally, momentum exchange devices can be used to control the orientation of a spacecraft, potentially eliminating the use of propellant. The rotation-flying control mode is an excellent compromise between range and control effort.

It is also important to note that for the rotation-flying and flying cases the actuators of the base-spacecraft can saturate. To ensure that they stay within their limits, the velocity of the end-effector can be limited to cap the base-reaction and thus reduce the instantaneous forces and torques required to compensate it (the required cumulative impulse will still be the same).

The manipulator configurations shown in Fig. 6 are provided in Table 4.

3.5. Determining the location of the hold positions

With all the different guidance and control laws employed during the different phases covered, the only remaining element to outline is how the different hold positions at the end of *Ph*.1 and *Ph*.3 are determined.

Table 5
Initial distance from the end-effector to the FSS docking target at the beginning of the final capture phase *Ph*.4.

	Distance
Stable FSS—Floating base	11.1 cm
Stable FSS—Flying base	23.4 cm
Stable FSS—Rotati-flying base	16.8 cm
Rotating FSS—Flying base	23.4 cm

Table 6
Hold position offsets.

Base control	Hold position offsets
Initial hold (end of *Ph*.1)	
Floating	$\Delta r_x = 1.54$ m, $\Delta r_y = -0.47$ m, $\Delta\theta = -63.68°$
Flying	$\Delta r_x = 1.60$ m, $\Delta r_y = -0.11$ m, $\Delta\theta = -50.71°$
Rotation-flying	$\Delta r_x = 1.53$ m, $\Delta r_y = -0.11$ m, $\Delta\theta = -50.71°$
Pre-capture hold (end of *Ph*.3)	
Floating	$\Delta r_x = 1.47$ m, $\Delta r_y = -0.35$ m, $\Delta\theta = 157.89°$
Flying	$\Delta r_x = 1.46$ m, $\Delta r_y = 0.02$ m, $\Delta\theta = 175.92°$
Rotation-flying	$\Delta r_x = 1.39$ m, $\Delta r_y = 0.02$ m, $\Delta\theta = 175.92°$

The hold positions are determined in a backwards order. First, the pre-capture hold position is determined. From that information the initial hold position is determined, taking into account the base-reaction occurring during the unfold maneuver.

The manipulator configuration used during the capture maneuver is selected first. For the experimental evaluation campaign, the configurations shown in Fig. 6, offering the "maximum" straight-line range, are selected.

The pre-capture hold position, reached at the end of *Ph*.3, is set in order to position the end-effector at a distance away from the target FSS equal to a third of the manipulator's maximum predicted range (see Fig. 6 for range data). This initial distance is tabulated in Table 5. Additionally, this hold position will have the end-effector pointing towards the target FSS.

With this arrangement, the end-effector only needs to move, nominally in a straight line, a third of its predicted range in order to capture the target FSS. The large range margin helps to compensate any starting position inaccuracies, such as, base-spacecraft residual velocity, measurement noise, imperfect manipulator or base-spacecraft actuation, modeling uncertainty, and the adverse effects of contact dynamics during the last centimeters of the capture (docking interface friction).

With the pre-capture position set, the nominal position to be reached after the manipulator is unfolded at the end of *Ph*.2 can be determined. This position is the same as the pre-capture hold position but increasing the distance to the target FSS by 20 cm. This extra distance ensures a collision-free manipulator unfolding. These extra 20 cm, along with any other residual misalignment, are corrected during the final approach phase *Ph*.3.

Finally, the estimated manipulator unfolding base-reaction is subtracted from the position to be achieved after the unfold maneuver, obtain the initial hold position targeted during *Ph*.1.

The hold positions are computed as offsets from the target FSS position $\boldsymbol{q}_0^{\text{target}}$ as follows:

$$\boldsymbol{q}_{0,\text{hold}} = \boldsymbol{q}_0^{\text{target}} + \begin{bmatrix} \boldsymbol{R} & \boldsymbol{0}_{2\times 1} \\ \boldsymbol{0}_{1\times 2} & 1 \end{bmatrix} \begin{bmatrix} \Delta r_x \\ \Delta r_y \\ \Delta\theta \end{bmatrix} \tag{19a}$$

$$\boldsymbol{R} = \begin{bmatrix} \cos\theta^{\text{target}} & -\sin\theta^{\text{target}} \\ \sin\theta^{\text{target}} & \cos\theta^{\text{target}} \end{bmatrix} \tag{19b}$$

with the values Δr_x, Δr_y, and $\Delta\theta$ tabulated in Table 6.

Table 7
Selected Floating Spacecraft Simulator parameters [21].

Parameter	Value
Mass	13 kg
Inertia	0.28 kg m^2
Dimensions (length × width)	0.27 × 0.27 m
Force per thruster	∼0.15 N (inlet pressure dependent)
Reaction wheel model	Ball Aerospace RW-2.5-A1
Reaction wheel max. angular momentum	±2.5 N m s
Reaction wheel mean max. torque	±53.2 mN m
Air tank capacity	1.868 cm^3 (14 ci)
Air tank nominal pressure	20.7 MPa (3000 psi)
Air bearings & thrusters nominal inlet pressure	413.7 Pa (60 psi)
Onboard CPU	Intel® Atom™ 1.6 GHz Z530 processor with 2 GB of RAM
Real-time operating System	Linux 2.6 with the `RT_PREEMPT` patch [47]
FOG	KVH® DSP-3000
Test bed residual linear acceleration $\ddot{r}$	$\sim 1.871\times10^{-4}$ m/s^2 (or ∼19.1 µg)
Test bed residual angular acceleration $\ddot{\theta}$	$\sim 7.56\times10^{-2}$ deg/s^2

4. Experimental setup

A brief overview of the POSEIDYN test bed and its test vehicles is provided in this section for completeness. See Fig. 1 for an overview of the experimental setup and refer to [21] for a more comprehensive description of the test bed.

4.1. Floating Spacecraft Simulators (FSS)

Each of the FSS hosts a single onboard tank of compressed air, which feeds three planar air bearings. When supplied with compressed air, the air bearings lift the FSS ∼5 µm above the granite table, greatly reducing the FSS friction. This quasi-frictionless dynamics combined with the horizontally leveled table produce a low residual acceleration environment in two translation and one rotation degree of freedom (planar motion).

Eight cold-gas thrusters [46], also fed by the onboard tank, provide autonomous motion capabilities to the FSS. On the chaser vehicle a reaction wheel provides additional torque actuation. This set of actuators replicates the common actuators found in actual spacecraft.

An onboard power system and an onboard computer make the FSS fully autonomous. A Wi-Fi module allows the FSS to communicate with other FSS or external equipment [48,49]. Selected parameters of the FSS are provided in Table 7.

An overhead motion capture system (VICON) is used to provide, at a 100 Hz rate, position and orientation measurements of the different FSS, rendering the navigation problem effectively solved. Streamed to the FSS via User Datagram Protocol (UDP) packets, the navigation data is augmented by an onboard Fiber Optic Gyroscope (FOG) and fused by a Discrete Kalman Filter (DKF), eventually resulting in a full state estimate ($\boldsymbol{q}_0$ and $\dot{\boldsymbol{q}}_0$).

4.2. Robotic manipulator

A custom developed modular four-link manipulator is mounted on the chaser FSS (see Fig. 1) [36]. Each of the manipulator links contains a single revolute joint actuated by an harmonic drive motor, with its associated driver and encoder. A torque sensor, an onboard computer (with a Wi-Fi module for connectivity), and a power system complete the link's onboard equipment (see Fig. 8). One air bearing per link ensures that the multibody system remains quasi-frictionless on the granite monolith. The FSS acting as the base-spacecraft supplies the compressed air to the links' air bearings.

Unlike the base-spacecraft navigation ($\boldsymbol{q}_0$ and $\dot{\boldsymbol{q}}_0$), which is partially solved with the aid of the overhead motion capture system, the manipulator state is measured using the manipulator's onboard sensors. These sensors provide the joint angular displacements $\boldsymbol{q}_m$ and the joint angular speed $\dot{\boldsymbol{q}}_m$. These measurements are fed to the kinematic and dynamic models used to derive the inertia matrices $\boldsymbol{H}$ and $\boldsymbol{C}$, Jacobians $\boldsymbol{J}_0$ and $\boldsymbol{J}_m$, as well as end-effector's position $\boldsymbol{q}_{EE}$ and velocity $\boldsymbol{t}_{EE}$. These derived magnitudes are used to control the vehicle as discussed in Section 3.

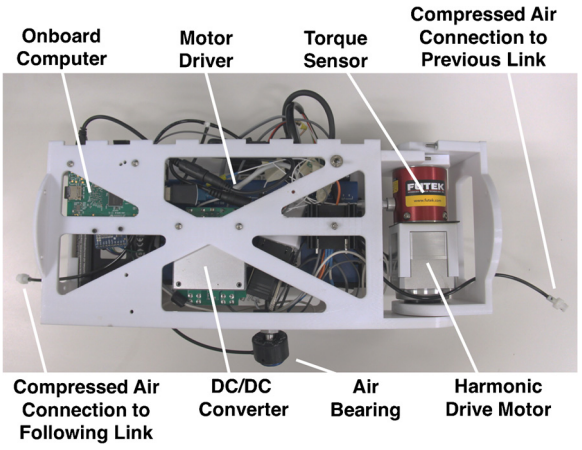

Fig. 8. A link of the modular manipulator.

Table 8
Selected manipulator parameters.

Parameter	Value
Mass per link	2.9 kg
Inertia per link	≈0.0364 kg m^2
Docking interface mass	0.2 kg
Last link's inertia	≈0.0385 kg m^2
Link's length (axis-to-axis)	0.38 m
Link's width	0.08 m
Motor max. torque	±1.8 N m
Absolute encoder resolution	150″
Torque sensor range	±2 N m
Max. joint angular displacement	± 90°
Control and telemetry rate	50 Hz

A conic docking interface, as shown in Fig. 9, is used for grappling the target FSS by the manipulator. An opposing pair of magnets, on the tip of both docking interfaces, provide latching when the capture is completed.

Given that the navigation problem is solved and that the RSO has a grappling fixture—in this case a docking interface—the target FSS can be considered as cooperative. This disposition is similar to the one used by the ASTRO chaser and its NextSat target during the Orbital Express mission [26,27]. Selected parameters of the robotic manipulator are provided in Table 8.

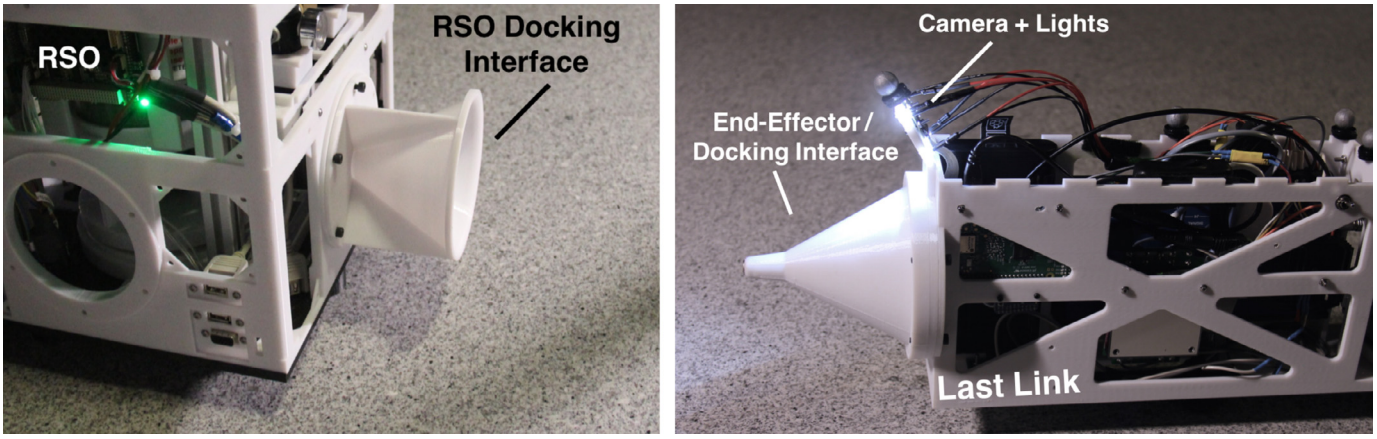

(a) Target FSS (b) Chaser's manipulator

Fig. 9. Docking interfaces.

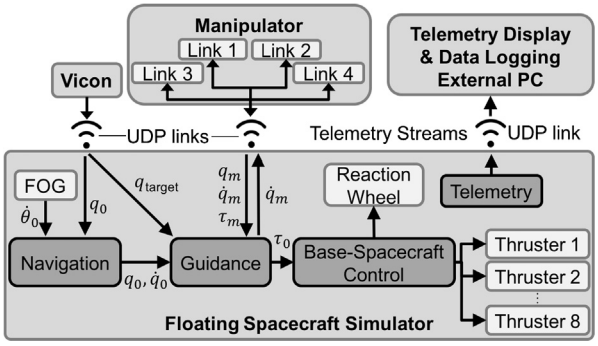

Fig. 10. Schematic of the spacecraft–manipulator system software architecture.

4.3. Onboard software

The onboard computer on the FSS, with its real-time operating system, handles all the required computations. A schematic representation of the FSS onboard software is shown in Fig. 10. To interact with the other elements of the test-bed, the onboard computer receives and sends UDP data streams over Wi-Fi. To communicate with the manipulator links, the base-spacecraft also uses UDP data streams over Wi-Fi. Each link streams its joint state–joint angular displacement ϕ_i, joint velocity $\dot{\phi}_i$ and joint torque n_i—and accepts joint velocity commands at a rate of 50 Hz. This telemetry and command rate drives the control algorithms presented in Section 3 to run at 50 Hz. The base-spacecraft position and attitude measurements provided by the VICON system are also received via a UDP stream over Wi-Fi. The target FSS state is also streamed to the base-spacecraft. Finally, the chaser FSS sends selected telemetry streams back to an external PC for debugging and logging purposes.

The navigation block contains the interfaces to acquire the VICON and FOG data, which is then fused in a DKF. The guidance block processes the base-spacecraft state $\boldsymbol{q}_0$ and $\dot{\boldsymbol{q}}_0$, the state of the target $\boldsymbol{q}_{\text{target}}$, and the telemetry streams coming from the manipulator in order to provide commands to the manipulator, in terms of joint angular velocities $\dot{\boldsymbol{q}}_m$, and to provide the generalized forces to be applied to the base-spacecraft $\boldsymbol{\tau}_0$. The base-spacecraft generalized forces are then parsed and mapped to the eight thrusters and the reaction wheel.

The base-spacecraft torque to be actuated n_0 is first commanded to the reaction wheel. The torque actuated by the reaction wheel n_{RW} is estimated from the reaction wheel's telemetry. Thrusters compensate for any difference between the requested torque n_0 and the torque actuated by the reaction wheel n_{RW}.

Table 9
Reaction wheel's controller parameters.

Parameter	Value
Flywheel's inertia J_{RW}	0.0102 kg m^2
Gain k_{RW}	1

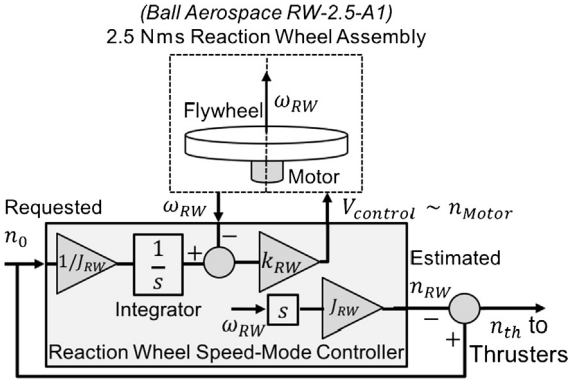

Fig. 11. Reaction wheel's speed-mode controller. Any torque not actuated by the reaction wheel is commanded to the thrusters.

This scheme, notionally shown in Fig. 11, ensures that the reaction wheel is used to its full extent before starting to use the thrusters, thus reducing the propellant consumption.

The reaction wheel is controlled via a speed-mode controller, while, given the discrete nature of the thrusters, a Sigma-Delta Modulator ($\Sigma\Delta$M) is used to actuate the commanded thrusters force [50].

A notional version of the reaction wheel's speed-mode controller is shown in Fig. 11, with ω_{RW} denoting the reaction wheel's angular velocity, J_{RW} the reaction wheel's inertia, and k_{RW} the speed-mode controller gain, which produces a voltage that determines the reaction wheel's motor torque n_{Motor}. The numerical values of these parameters are provided in Table 9. The implemented controller is significantly more complex than the one depicted in Fig. 11, as it contains a spool up mode, (used to get the reaction wheel up to its nominal speed), an angular velocity filter, a maximum reaction wheel rate protection, and a saturation control that eliminates integral windup. The $\Sigma\Delta$M topology is shown in Fig. 12, with k_{DAC} taking the value of the thruster force detailed in Table 7.

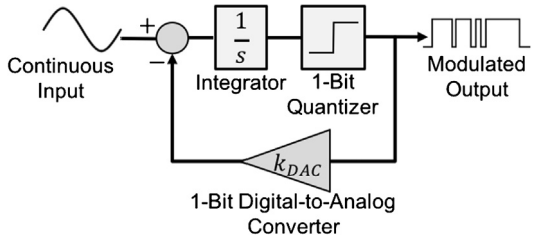

Fig. 12. Sigma-Delta Modulator topology [50].

Table 10
Initial conditions.

Parameter	Value
Chaser FSS initial condition	$r_{0x} = 3.5$ m, $r_{0y} = 2$ m, $\theta_0 = 0°$
Manipulator's folded configuration	$\boldsymbol{q}_m = [-85°, -85°, -85°, -15°]$
Target FSS at rest	
Target FSS position	$r_x^{\text{target}} = 0.5$ m, $r_y^{\text{target}} = 0.5$ m, $\theta^{\text{target}} = 45°$
Rotating target FSS	
Target FSS position	$r_x^{\text{target}} = 0.5$ m, $r_y^{\text{target}} = 0.5$ m
Target FSS angular velocity	$\dot{\theta}^{\text{target}} = 0.5°/s$
Chaser FSS starts maneuver when	$\theta^{\text{target}} \geq 15°$

5. Experimental results

Using the controllers presented in Section 3 and the test vehicles operating in POSEIDYN test bed as described in Section 4, the capture of a target at rest and a rotating target has been experimentally demonstrated.

For the target at rest scenario, the three different base-spacecraft control modes for the final capture phase *Ph.*4 have been tested. Ten experiments for each control mode have been carried out. For the rotating target scenario only a flying base control has been experimentally demonstrated. Ten experiments have been also carried out for this case. The initial conditions of the chaser and the target are provided in Table 10.

For a rotating target, using a flying base ensures that the base-spacecraft tracks the target FSS rotation during the capture maneuver. The end-effector nominal capture trajectory remains a straight-line approach, as in the target at rest scenario, allowing reuse of the guidance and control laws developed for the target at rest scenario. A floating or rotation-flying control mode could potentially be employed in a rotating target scenario, albeit several changes to the control laws would be necessary. In these other control modes, the base-spacecraft would no longer track the target FSS, getting-out-of-sync during the capture maneuver and thus rendering the originally planned straight-line end-effector approach unusable. New manipulator initial configurations would be required to ensure that the end-effector could track this new trajectory.

Figs. 13–16 show the experimental results of the tests conducted on the POSEIDYN test bed for each of the tested cases. The subfigures in Figs. 13–16 show a snapshot of the state of the system at the end of each maneuver phase, with the solid and dashed lines indicating the path traversed by the system's center-of-mass during the individual experiments and the mean center-of-mass path, respectively. The mean path is computed as the locus of the individual experiments center-of-mass positions at the same maneuver completion percentage. The chaser and target configurations shown in Figs. 13–16 represent the mean state at the end

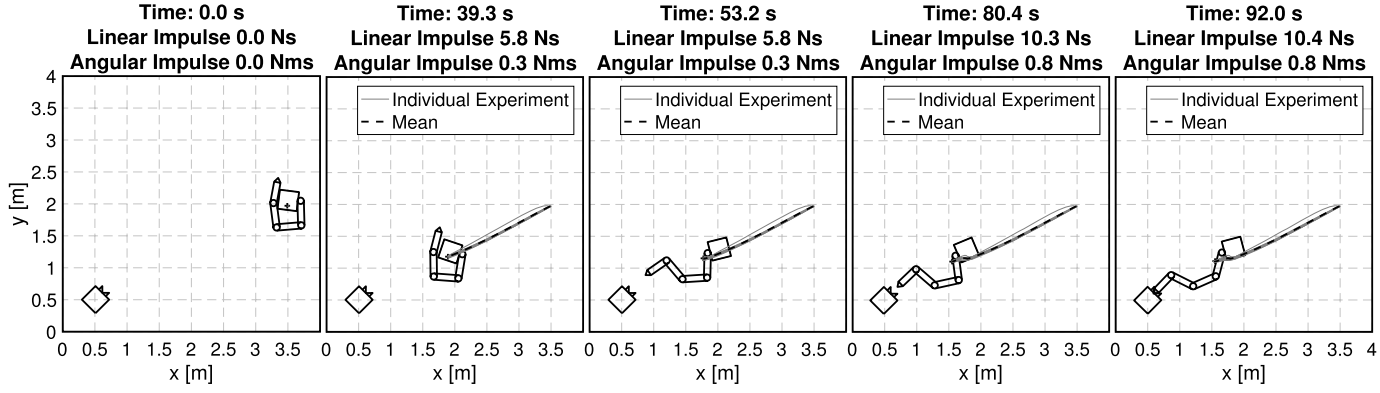

(a) Initial condition (b) Initial hold position (c) Manipulator unfolded (d) Pre-capture hold (e) Captured FSS target

Fig. 13. Experimental results for a floating base control during the *Ph.*4 of the capture of a target FSS at rest.

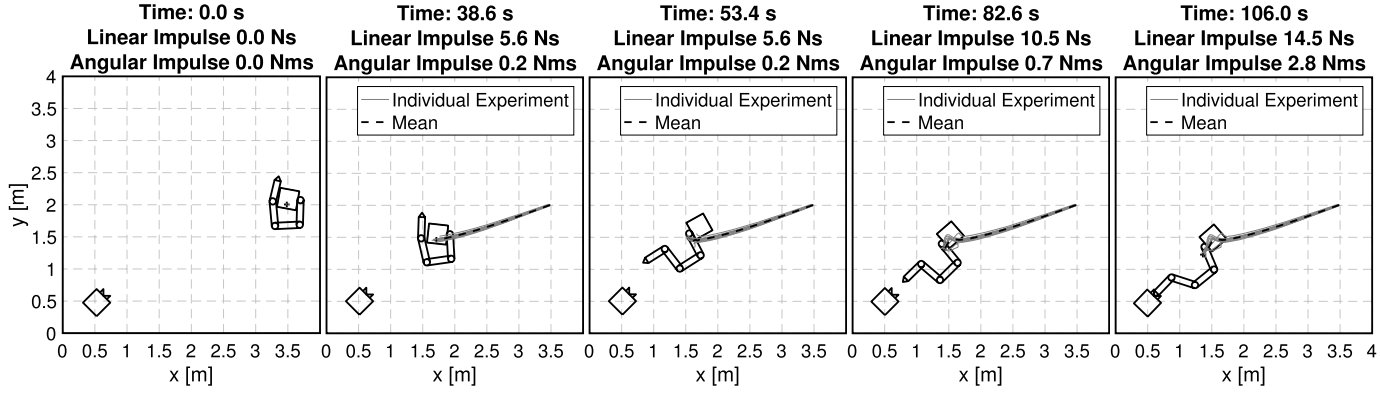

(a) Initial condition (b) Initial hold position (c) Manipulator unfolded (d) Pre-capture hold (e) Captured FSS target

Fig. 14. Experimental results for a flying base control during the *Ph.*4 of the capture of a target FSS at rest.

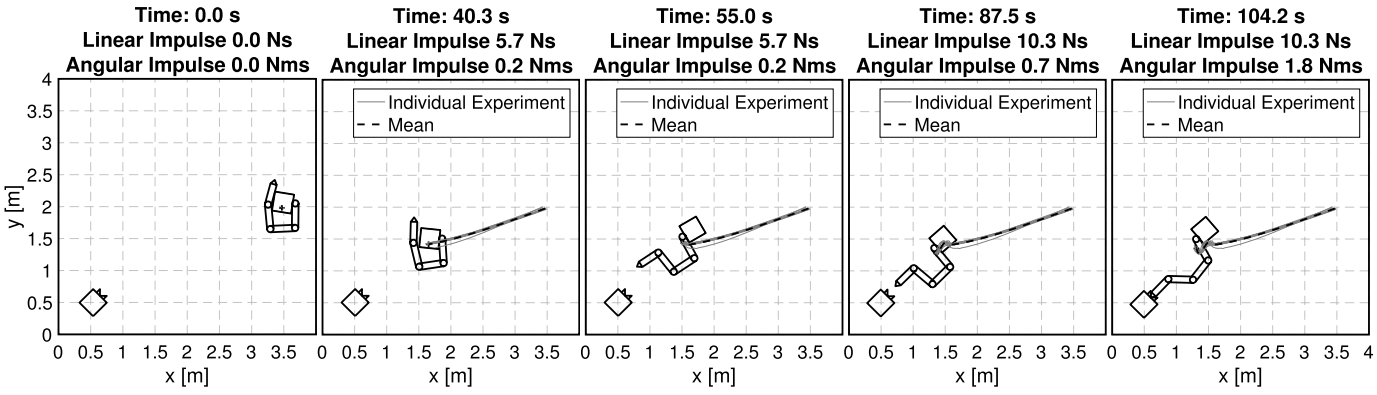

(a) Initial condition (b) Initial hold position (c) Manipulator unfolded (d) Pre-capture hold (e) Captured FSS target

Fig. 15. Experimental results for a rotation-flying base control during the *Ph.*4 of the capture of a target FSS at rest.

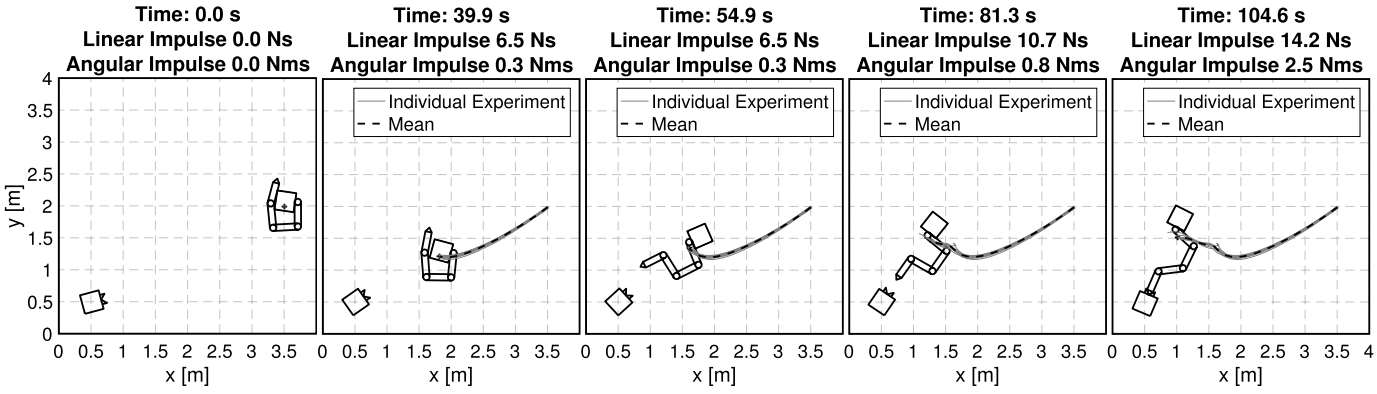

(a) Initial condition (b) Initial hold position (c) Manipulator unfolded (d) Pre-capture hold (e) Captured FSS target

Fig. 16. Experimental results for a flying base control during the *Ph.*4 of the capture of a rotating target FSS.

of that maneuver phase. The cumulative maneuver time as well as the commanded linear and angular impulses are also shown in Figs. 13–16.

For the rotating target case, the target FSS is rotating at a constant 0.5°/s. The angular velocity of the target is physically limited by the amount of space available in the POSEIDYN test bed. With an angular rate of 0.5°/s the chaser has enough time to complete the maneuver before running out of space on the test bed.

The linear and angular impulse commanded is used as an indicator of the maneuver's control effort. Figs. 17(b) and 17(c) provide an overview of the impulses commanded in each maneuver phase, with the bars showing the mean impulse over the ten experiments and the error bars showing the 1σ standard deviation on these measurements. For comparison, the results obtained using a numerical simulator are also presented along the experimental results. For the numerical simulations, the navigation errors have been modeled and the statistics over ten simulations are collected and displayed. Similarly, the time to complete the different maneuver phases is provided in Fig. 17(a).

Fig. 18 shows the end-effector capture trajectories. To display the target FSS in Fig. 18, its mean end-state is used. The chaser's manipulator, corresponding to the mean initial configuration, is also displayed for reference.

The base-spacecraft commanded forces τ_0 are provided in Fig. 19, with the results of the first test highlighted with a bolder line. The different maneuver phases marked in Fig. 19 are based on the highlighted test. On the base-spacecraft torque n_0 plots, the maximum and minimum reaction wheel torque are marked with dashed lines. These force figures help visualize the differences between the base control modes.

It is also interesting to look at the center-of-mass and base-spacecraft (r_{0x} and r_{0y}) displacements during the final capture phase *Ph.*4. These displacements are shown in Fig. 20. The chaser FSS is shown in Fig. 20, with its mean initial configuration, for reference.

As a supplementary material, the video showing the telemetry replays for all the experiments is provided. An additional experiment for each case has been recorded, with the resulting videos added as supplementary material.

6. Discussion

The results of the experimental campaign are analyzed and discussed in this section. Before starting the analysis, it is worth specifying that all 40 experiments—ten for each case—were successful. The experiments were conducted sequentially and with the same control software (only switching between base-spacecraft control modes during the final capture phase). No failures were registered during any of the experiments. The proposed capture approach and control laws appear to be robust and repeatable, compensating for the model uncertainties as well as for the navigation and actuation noise present on the POSEIDYN-based experimental setup.

By analyzing the linear and angular impulses (proxies of the control effort) used for each control mode, shown in Figs. 17(b) and 17(c), several conclusions can be drawn. First, it can be noted that the linear and angular impulse used for the initial approach phase *Ph.*1 is similar for all the different *Ph.*4 control modes. The position and attitude differences in the initial hold position are small and do not seem to have a major impact on the required control effort. Only the case targeting a rotating FSS, where the

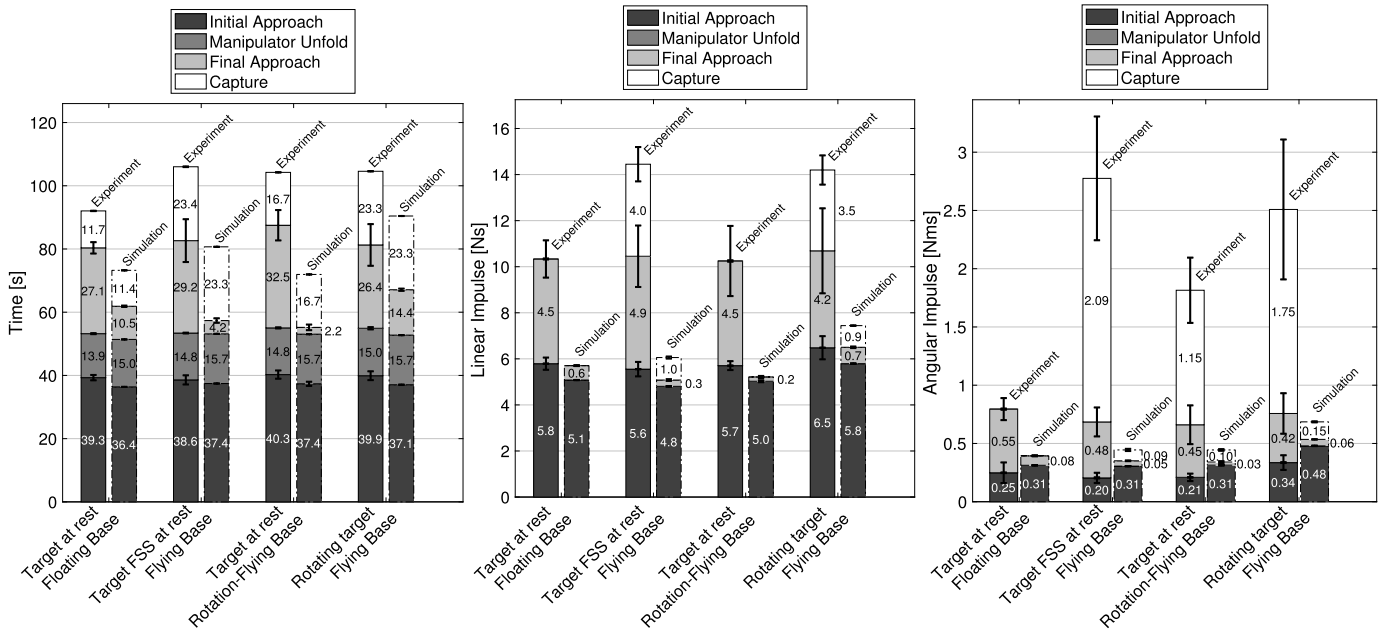

(a) Time elapsed in each maneuver phase. (b) Linear impulse commanded in each maneuver phase. (c) Angular impulse commanded in each maneuver phase.

Fig. 17. Statistics.

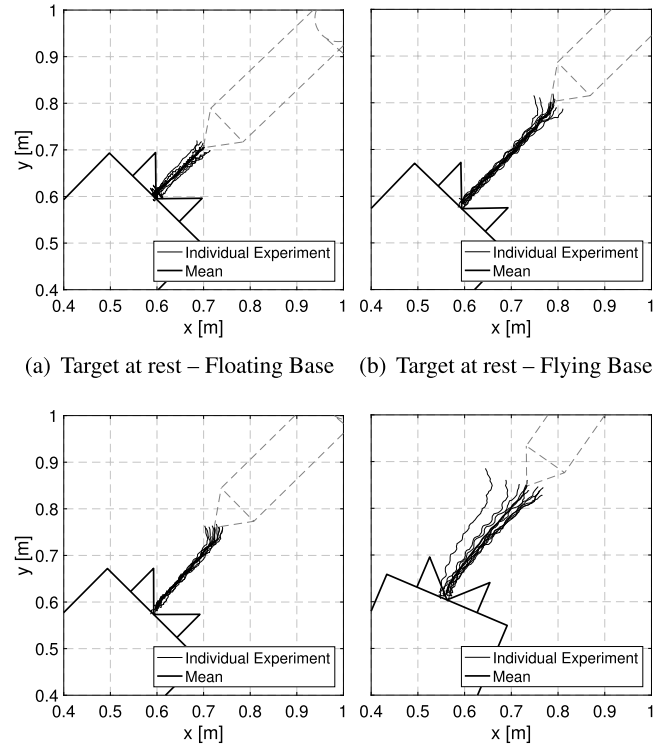

(a) Target at rest – Floating Base (b) Target at rest – Flying Base

(c) Target at rest – Rotating-Flying Base (d) Rotating target– Flying Base

Fig. 18. End-effector trajectories during the final capture *Ph*.4.

hold position tracks the rotating target, requires slightly higher impulses. This is an expected result, since in all cases the roto-translation is conducted with the same manipulator configuration (folded) and using the same LQR controller. Also, the results from the experimental campaign match quite well the results obtained using numerical simulations. The main difference is that the experiments show a much higher dispersion. The higher dispersion observed on the experimental results is a constant on all the results, with its potential causes addressed later. It is also worthy to note that the *Ph*.1 angular impulse commanded during the experiments is consistently lower than the one predicted by the numerical simulations. The root cause of this discrepancy has not been investigated in detail, but potential inaccuracies on the estimated bodies inertia and center-of-mass locations are likely candidates. The time required to complete this first phase, shown in Fig. 17(a), is also similar across all cases, matching the predictions given by the numerical simulations.

Table 11
End-effector misalignment after completing the manipulator unfold maneuver.

	Mean	Standard deviation
Target FSS at rest—Floating base	10.02°	1.83°
Target FSS at rest—Flying base	12.74°	4.95°
Target FSS at rest—Rotating-flying base	11.54°	1.35°
Rotating target FSS—Flying base	15.78°	2.16°

The unfold maneuver in *Ph*.2 is conducted, in all cases, using a floating base, thus not exerting any control effort on the base-spacecraft. The time taken to complete this maneuver is, as expected, consistent and matches the predictions from the numerical simulations. As seen in Figs. 13–16, after the unfold maneuver is completed, the chaser FSS is roughly aligned with its target, proving that the base-reaction is correctly anticipated. Nonetheless, a consistent ∼10° misalignment bias is observed at the end of the unfold maneuver, as detailed in Table 11. This misalignment bias may be indicative of a small, yet systematic, difference between the simulated and experimental unfold maneuver (how the manipulator joints move with respect to each other), or within the dynamic model of the chaser system (*i.e.*, inaccuracies on the masses, inertias and centers-of-mass of the different bodies).

The misalignment of the unfold maneuver is corrected during the final approach *Ph*.3. During this phase the translation and angular impulse used by all three cases is again similar. All cases use the same LQR controller, with different manipulator configurations, and the distances to be traversed are (nominally) identical. The dif-

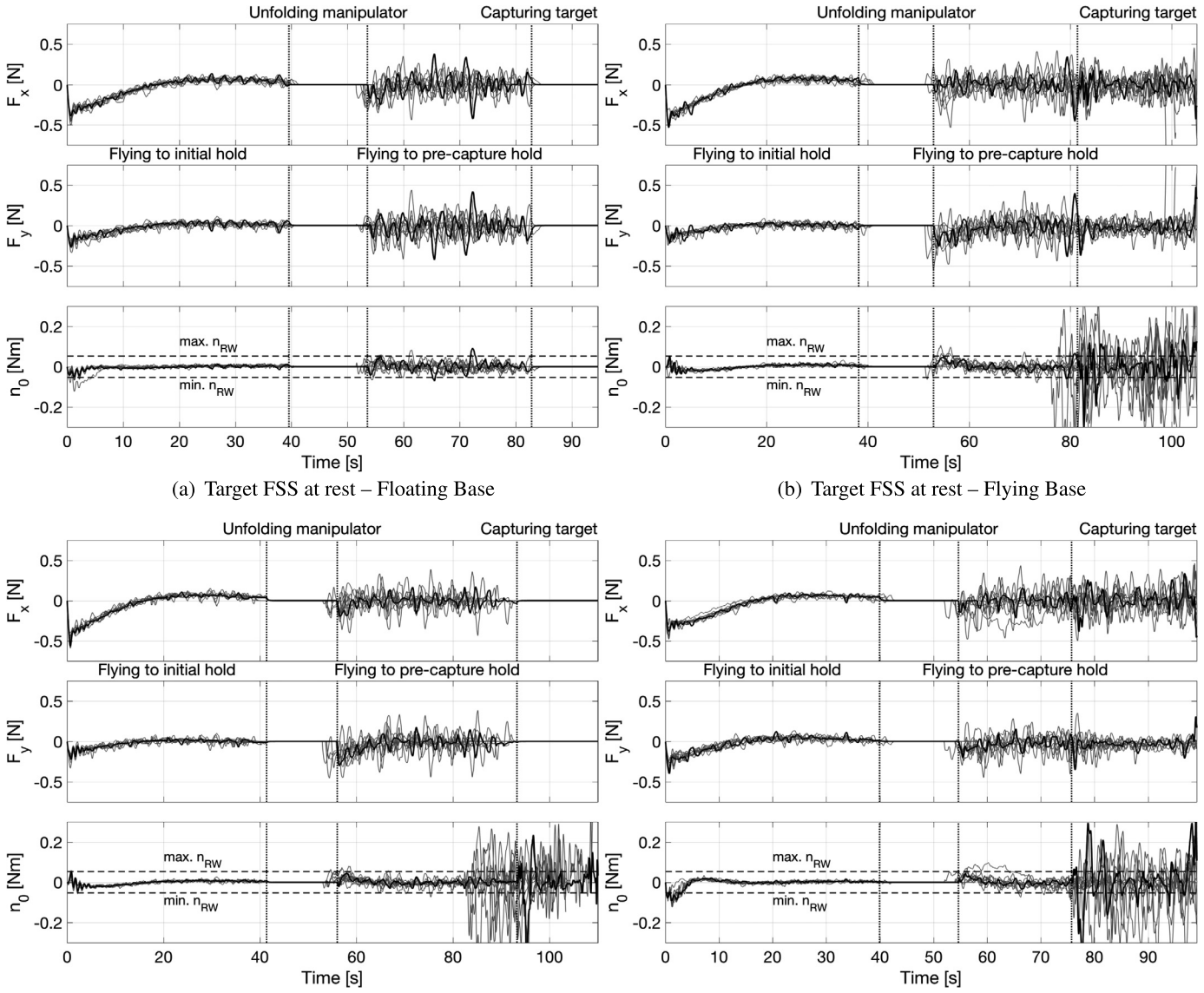

(a) Target FSS at rest – Floating Base

(b) Target FSS at rest – Flying Base

(c) Target FSS at rest – Rotation-Flying Base

(d) Rotating target FSS – Flying Base

Fig. 19. Base-spacecraft forces.

ference between the numerical simulations and the experiments for this phase are quite large. Also, the dispersion on the translation and angular impulses as well as in the maneuver duration is much larger than the ones observed for *Ph*.1. The main reason for discrepancy and larger dispersion is found on the more aggressive LQR controller used in this phase and the observed flexibility of the unfolded manipulator. The manipulator links and joints are slightly flexible. This flexibility is difficult to notice on a single link, but when the four links are arranged in a serial configuration the manipulator's flexibility is quite apparent. The flexible manipulator tends to oscillate when the thrusters fire, dissipating energy and causing an oscillation on the base-spacecraft's position that the LQR attempts to correct. The result: a higher thruster actuation as well as a longer and less predictable maneuver. In Fig. 19 the base-spacecraft's force $\boldsymbol{\tau}_0$ oscillations caused by the manipulator flexibility can be clearly seen. During the initial approach *Ph*.1, this oscillating effect was not as severe as the LQR controller was less aggressive, with a larger threshold (see Table 2), and the manipulator was in its folded configuration, reducing the thrusters' lever arm.

During the final capture phase *Ph*.4, the main differences in impulse among the different cases arise. In the floating and rotation-flying case no translation control is used, whereas a significant amount is employed in the flying case. The floating base control approach is the only one that does not command any angular impulse. As in the final approach, the flexibility of the manipulator causes a higher impulses than predicted by the numerical simulations. It is also worth noting that despite using a rotation-flying base control the FSS thrusters are used to complement the reaction wheel, thus still inducing oscillations.

During the final capture phase the manipulator's end-effector captures the target. From the results shown in Fig. 18, it is clear that the end-effector is able to track its desired straight-line trajectory. During the experiments using a rotating FSS, the end-effector trajectory appears slightly curved as the target and chaser are moving during this final capture phase. The good tracking performance significantly reduces the friction between the two ends of the docking interface, minimizing the disturbance on the target or chaser caused by the contact dynamics. Another indication of the good tracking performance is given by the duration of the capture maneuver, nearly equal to the simulation predictions and to

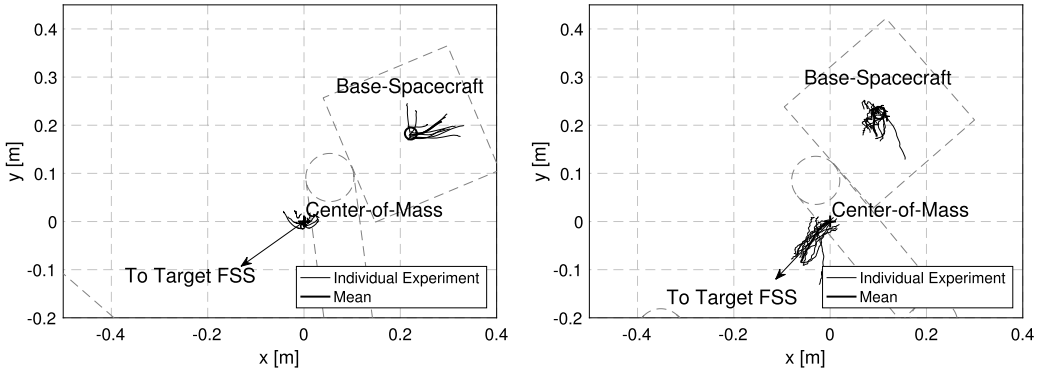

(a) Target FSS at rest – Floating Base

(b) Target FSS at rest – Flying Base

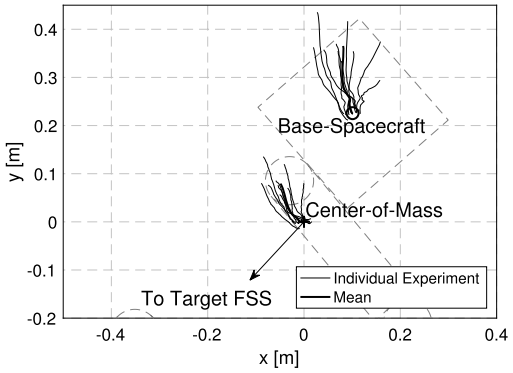

(c) Target FSS at rest – Rotating-Flying Base

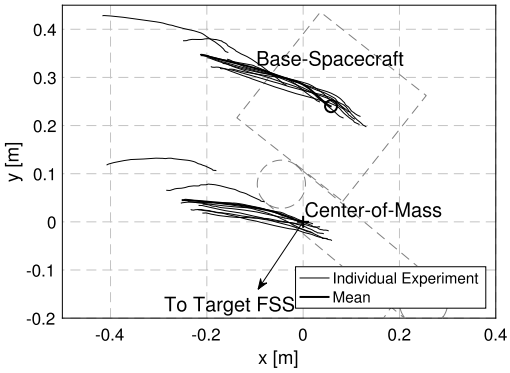

(d) Rotating target FSS – Flying Base

Fig. 20. Chaser FSS center-of-mass displacement during the final capture maneuver (coordinates with respect to the mean initial center-of-mass location).

the ideal maneuver time. The minimal dispersion of the capture is an additional indication of this good performance. In an ideal capture maneuver, the end-effector would be moving at a 1 cm/s (see Section 3.4.1) along a straight line with a length specified in Table 5. Despite the end-effector controller, the manipulator's flexibility does also induce an oscillation on the end-effector position, as seen in Fig. 18. Additionally, in Fig. 18 the differences in initial end-effector distance between the different base control modes (driven by their different capture ranges) are evident.

Another result to analyze is the displacements of the chaser's center-of-mass and base-spacecraft position during the capture maneuver. These displacements are shown in Fig. 20. The results from the floating base and flying base control modes are as expected. For a floating base, the center-of-mass position should remain constant (as no translation momentum is imparted to the system), while the base position should move away from the target (compensating the manipulator's motion). This can be seen in Fig. 20. In contrast, with a flying base, the thrusters impart a linear momentum in order to keep the base fixed, and consequently, a center-of-mass translation towards the target is expected. The results in Fig. 20 show this expected behavior.

Although the mean center-of-mass displacement during the floating base capture maneuvers is negligible, the individual experiments show a small center-of-mass displacement. This displacement can be attributed to residual motion at the end of *Ph*.3 and to model inaccuracies when estimating the system's center-of-mass.

The results of the rotation-flying base experiments do not show the expected behavior. In this case, the center-of-mass position should remain constant and the base-spacecraft position should move away (in a similar manner as when using a floating base). In the rotation-flying base results, the base moves away but the center-of-mass also moves a significant amount. This discrepancy can be attributed to the FSS thrusters. When using a rotation-flying base, the base-spacecraft rotation is controlled while its position is left to freely react. To control its rotation the base-spacecraft commands the reaction wheel, complemented by the thrusters, to actuate the desired torques. To generate a pure torque, with ideally no residual translation force, four thrusters are fired. The thrusters are not perfectly aligned, and a thruster-to-thruster force variation does exist [21]. This may result in residual translation forces, imparting linear momentum and displacing the system's center-of-mass. Using the FSS reaction wheel as the only actuator employed to actuate the desired torques could potentially eliminate this adverse effect, although the end-effector velocity would need to be significantly reduced in order to keep the reaction torques within the reaction wheel's torque envelope.

The flexibility of the manipulator causes the system to diverge from the expected behavior. This difference serves as a reminder of the importance of the role of ground-based test beds during the development and validation of new guidance and control algorithms.

7. Conclusions

This paper reports the experimental demonstration, in a laboratory environment, of the capture of a resident space object simulator at rest as well as rotating by a spacecraft simulator equipped with a kinematically redundant robotic manipulator. The high dynamic coupling of the spacecraft–manipulator system used, gives to these demonstrations a special relevance. These experiments provide empirical evidence that these highly coupled systems can be controlled and used to capture resident space objects of similar mass. Despite the limited number of experiments conducted—ten per case, 40 in total—the proposed approach and proposed guidance and control laws proved to be robust and repeatable, successfully capturing the target object in all the conducted experiments. The good tracking performance of the end-effector during the final capture phase minimized undesired disturbances caused by

contact dynamics. The manipulator's flexibility induced unwanted oscillations during the "powered" phases of the maneuver, significantly increasing the propellant expenditure when compared to the numerical simulation predictions. This dynamic effect, difficult to model on a numerical simulation environment, illustrates the need and relevance of ground-based hardware-in-the-loop test beds.

Conflict of interest statement

There is no conflict of interest.

Appendix A. Supplementary material

Supplementary material related to this article can be found online at https://doi.org/10.1016/j.ast.2017.09.043.

References

[1] S.A.A. Moosavian, E. Papadopoulos, Free-flying robots in space: an overview of dynamics modeling, planning and control, Robotica 25 (2007) 537–547, http://dx.doi.org/10.1017/S0263574707003438.

[2] W. Xu, B. Liang, Y. Xu, Survey of modeling, planning, and ground verification of space robotic systems, Acta Astronaut. 68 (11–12) (2011) 1629–1649, http://dx.doi.org/10.1016/j.actaastro.2010.12.004.

[3] A. Flores-Abad, O. Ma, K. Pham, S. Ulrich, A review of space robotics technologies for on-orbit servicing, Prog. Aerosp. Sci. 68 (2014) 1–26, http://dx.doi.org/10.1016/j.paerosci.2014.03.002.

[4] J.L. Schwartz, M.A. Peck, C.D. Hall, Historical review of air-bearing spacecraft simulators, J. Guid. Control Dyn. 26 (4) (2003) 513–522.

[5] T. Rybus, K. Seweryn, Planar air-bearing microgravity simulators: review of applications, existing solutions and design parameters, Acta Astronaut. 120 (2016) 239–259, http://dx.doi.org/10.1016/j.actaastro.2015.12.018.

[6] H.L. Alexander, R.H. Cannon, Experiments on the Control of a Satellite Manipulator, Springer, Berlin, Heidelberg, 1989, pp. 93–105.

[7] Y. Umetani, K. Yoshida, Experimental study on two-dimensional free-flying robot satellite model, in: Proceedings of NASA Conference on Space Telerobotics, vol. 5, 1989, pp. 215–224.

[8] M.A. Ullman, R.H. Cannon, Experiments in Autonomous Navigation and Control of a Multi-Manipulator, Free-Flying Space Robot, Springer US, Boston, MA, 1993, pp. 269–284.

[9] V.W. Chen, R.H. Cannon, Experiments in nonlinear adaptive control of multi-manipulator free-flying robots, in: Proceedings of the IEEE International Conference Robotics and Automation, vol. 3, 1994, pp. 2213–2220.

[10] J. Russakow, O. Khatib, S.M. Rock, Extended operational space formulation for serial-to-parallel chain (branching) manipulators, in: Proceedings of the IEEE International Conference Robotics and Automation, vol. 1, 1995, pp. 1056–1061.

[11] K. Yoshida, Experimental study on the dynamics and control of a space robot with experimental free-floating robot satellite, Adv. Robot. 9 (6) (1994) 583–602, http://dx.doi.org/10.1163/156855395X00319.

[12] M. Nahon, C. Damaren, A. Bergen, J. Goncalves, A test facility for multi-armed space-based manipulators, Can. Aeronaut. Space J. 41 (4) (1995) 150–162.

[13] C. Menon, S. Busolo, S. Cocuzza, A. Aboudan, A. Bulgarelli, C. Bettanini, M. Marchesi, F. Angrilli, Issues and solutions for testing free-flying robots, Acta Astronaut. 60 (12) (2007) 957–965, http://dx.doi.org/10.1016/j.actaastro.2006.11.014.

[14] C. Toglia, F. Kennedy, S. Dubowsky, Cooperative control of modular space robots, Auton. Robots 31 (2–3) (2011) 209–221, http://dx.doi.org/10.1007/s10514-011-9238-z.

[15] M. Wilde, M. Ciarcià, A. Grompone, M. Romano, Experimental characterization of inverse dynamics guidance in docking with a rotating target, J. Guid. Control Dyn. 39 (6) (2016) 1173–1187, http://dx.doi.org/10.2514/1.G001631.

[16] S. Nishida, T. Yoshikawa, A robotic small satellite for space debris capture, in: IEEE International Conference on Robotics and Biomimetics, ROBIO 2008, 2009, pp. 1348–1353.

[17] D. Reintsema, B. Sommer, T. Wolf, J. Theater, A. Radthke, J. Sommer, W. Naumann, P. Rank, Deos–the in-flight technology demonstration of German's robotics approach to dispose malfunctioned satellites, in: ESA 11th Symposium on Advanced Space Technologies in Robotics and Automation, ESTEC, Netherlands, 2011.

[18] D.L. Akin, K.M. McBryan, N.M. Limparis, C.J. Carlsen, K.P. Davis, Miniature orbital dexterous servicing system, in: Proceedings of 12th International Symposium on Artificial Intelligence, Robotics and Automation in Space (i-SAIRAS 2014), Montreal, Canada, 2014.

[19] A. Ruggiero, P. Pergola, M. Andrenucci, Small electric propulsion platform for active space debris removal, IEEE Trans. Plasma Sci. 43 (12) (2015) 4200–4209, http://dx.doi.org/10.1109/TPS.2015.2491649.

[20] T. Rybus, T. Barciński, J. Lisowski, J. Nicolau-Kukliński, K. Seweryn, M. Ciesielska, K. Grassmann, J. Grygorczuk, M. Karczewski, M. Kowalski, et al., New planar air-bearing microgravity simulator for verification of space robotics numerical simulations and control algorithms, in: Proceedings of 12th Symposium on Advanced Space Technologies in Robotics and Automation, 2013.

[21] R. Zappulla II, J. Virgili-Llop, C. Zagaris, H. Park, M. Romano, Dynamic air-bearing hardware-in-the-loop testbed to experimentally evaluate autonomous spacecraft proximity maneuvers, J. Spacecr. Rockets 54 (4) (2017) 825–839, http://dx.doi.org/10.2514/1.A33769.

[22] J. Virgili-Llop, J. Drew, R. Zappulla II, M. Romano, Autonomous capture of a resident space object by a spacecraft with a robotic manipulator: analysis, simulation and experiments, in: AIAA/AAS Astrodynamics Specialist Conference, Long Beach, California, 13–16 September 2016, American Institute of Aeronautics and Astronautics, 2016.

[23] C. Sallaberger, S.P.T. Force, C.S. Agency, Canadian space robotic activities, Acta Astronaut. 41 (4–10) (1997) 239–246, http://dx.doi.org/10.1016/S0094-5765(98)00082-4, developing Business.

[24] M. Stieber, C. Trudel, D. Hunter, Robotic systems for the international space station, in: IEEE International Conference on Robotics and Automation, vol. 4, 1997, pp. 3068–3073.

[25] M. Oda, Experiences and lessons learned from the ets-vii robot satellite, in: IEEE International Conference on Robotics and Automation, 2000. Proceedings, ICRA '00, vol. 1, 2000, pp. 914–919.

[26] J. Shoemaker, M. Wright, Orbital express space operations architecture program, in: Defense and Security, International Society for Optics and Photonics, 2004, pp. 57–65.

[27] A. Ogilvie, J. Allport, M. Hannah, J. Lymer, Autonomous satellite servicing using the orbital express demonstration manipulator system, in: Proc. of the 9th International Symposium on Artificial Intelligence, Robotics and Automation in Space (i-SAIRAS'08), 2008, pp. 25–29.

[28] S. Jacobsen, C. Lee, C. Zhu, S. Dubowsky, Planning of safe kinematic trajectories for free flying robots approaching an uncontrolled spinning satellite, in: ASME 2002 International Design Engineering Technical Conferences and Computers and Information in Engineering Conference, American Society of Mechanical Engineers, 2002, pp. 1145–1151.

[29] R. Lampariello, Motion planning for the on-orbit grasping of a non-cooperative target satellite with collision avoidance, in: Int. Symp. Artif. Intell. Robot. Automat. Space, vol. 1, 2010, pp. 636–643.

[30] R. Lampariello, G. Hirzinger, Generating feasible trajectories for autonomous on-orbit grasping of spinning debris in a useful time, in: 2013 IEEE/RSJ International Conference on Intelligent Robots and Systems (IROS), IEEE, 2013, pp. 5652–5659.

[31] S.M. Persson, I. Sharf, Ground-based experiments towards the interception of non-cooperative space debris with a robotic manipulator, in: 2015 IEEE/RSJ International Conference on Intelligent Robots and Systems (IROS), 2015, pp. 5441–5446.

[32] A. Flores-Abad, L. Zhang, Z. Wei, O. Ma, Optimal capture of a tumbling object in orbit using a space manipulator, J. Intell. Robot. Syst. (2016) 1–13, http://dx.doi.org/10.1007/s10846-016-0417-1.

[33] J. Virgili-Llop, C. Zagaris, R. Zappulla II, A. Bradstreed, M. Romano, Convex optimization for proximity maneuvering of a spacecraft with a robotic manipulator, in: 27th AAS/AIAA Space Flight Mechanics Meeting, San Antonio, Texas, 5–9 February 2017, 2017.

[34] J. Virgili-Llop, D.V. Drew, M. Romano, Spacecraft robotics toolkit: an open-source simulator for spacecraft robotic arm dynamic modeling and control, in: 6th International Conference on Astrodynamics Tools and Techniques, 2016.

[35] J. Virgili-Llop, et al., SPART: spacecraft robotics toolkit, https://github.com/NPS-SRL/SPART.

[36] J. Virgili-Llop, J. Drew, M. Romano, Design and parameter identification by laboratory experiments of a prototype modular robotic arm for orbiting spacecraft applications, in: 6th International Conference on Astrodynamics Tools and Techniques (ICATT), 14–17 March 2016, Darmstadt, Germany, 2016.

[37] S.B. McCamish, M. Romano, X. Yun, Autonomous distributed control of simultaneous multiple spacecraft proximity maneuvers, IEEE Trans. Autom. Sci. Eng. 7 (3) (2010) 630–644, http://dx.doi.org/10.1109/TASE.2009.2039010.

[38] S.B. McCamish, M. Romano, S. Nolet, C.M. Edwards, D.W. Miller, Flight testing of multiple-spacecraft control on spheres during close-proximity operations, J. Spacecr. Rockets 46 (6) (2009) 1202–1213, http://dx.doi.org/10.2514/1.43563.

[39] T. Çimen, Survey of state-dependent Riccati equation in nonlinear optimal feedback control synthesis, J. Guid. Control Dyn. 35 (4) (2012) 1025–1047, http://dx.doi.org/10.2514/1.55821.

[40] D.E. Whitney, Resolved motion rate control of manipulators and human prostheses, IEEE Trans. Human-Mach. Syst. 10 (2) (1969) 47–53, http://dx.doi.org/10.1109/TMMS.1969.299896.

[41] Y. Umetani, K. Yoshida, Resolved motion rate control of space manipulators with generalized Jacobian matrix, IEEE Trans. Robot. Autom. 5 (3) (1989) 303–314, http://dx.doi.org/10.1109/70.34766.

[42] K. Yoshida, K. Hashizume, S. Abiko, Zero reaction maneuver: flight validation with ets-vii space robot and extension to kinematically redundant arm, in: IEEE International Conference on Robotics and Automation, 2001. Proceedings 2001 ICRA, vol. 1, 2001, pp. 441–446.

[43] A. Liegeois, Automatic supervisory control of the configuration and behavior of multibody mechanisms, IEEE Trans. Syst. Man Cybern. Syst. 7 (12) (1977) 868–871, http://dx.doi.org/10.1109/TSMC.1977.4309644.

[44] J. Snyman, Practical Mathematical Optimization: An Introduction to Basic Optimization Theory and Classical and New Gradient-Based Algorithms, vol. 97, Springer Science & Business Media, 2005.

[45] T. Peters, D. Escorial Olmos, Applicability of cobra concept to detumbling space debris objects, in: Proceedings of the 6th International Conference on Astrodynamics Tools and Techniques, 2016.

[46] C. Lugini, M. Romano, A ballistic-pendulum test stand to characterize small cold-gas thruster nozzles, Acta Astronaut. 64 (5) (2009) 615–625, http://dx.doi.org/10.1016/j.actaastro.2008.11.001.

[47] S. Arthur, C. Emde, N. Mc Guire, Assessment of the realtime preemption patches (rt-preempt) and their impact on the general purpose performance of the system, in: Proceedings of the 9th Real-Time Linux Workshop, 2007.

[48] M. Romano, D.A. Friedman, T.J. Shay, Laboratory experimentation of autonomous spacecraft approach and docking to a collaborative target, J. Spacecr. Rockets 44 (1) (2007) 164–173, http://dx.doi.org/10.2514/1.22092.

[49] R. Bevilacqua, J.S. Hall, J. Horning, M. Romano, Ad hoc wireless networking and shared computation for autonomous multirobot systems, J. Aerosp. Comput. Inf. Commun. 6 (5) (2009) 328–353, http://dx.doi.org/10.2514/1.40734.

[50] R. Zappulla II, J. Virgili-Llop, M. Romano, Spacecraft thruster control via sigma-delta modulation, J. Guid. Control Dyn. (2017), https://doi.org/10.2514/1.G002986 (in press).